INVITED REVIEW PAPERS

Core Excitation and De-excitation Spectroscopies
of Free Atoms and Molecules

Kiyoshi UEDA*

Institute of Multidisciplinary Research for Advanced Materials, Tohoku University, Sendai 980-8577

This article provides a review of the current status of core excitation and de-excitation spectroscopy studies of free atoms and molecules using a high-resolution soft X-ray monochromator and a high-resolution electron energy analyzer, installed in the soft X-ray photochemistry beam line at SPring-8. Experimental results are discussed for 1s excitation of Ne, O 1s excitation of CO and H_2O, and F 1s excitation of CF_4.

1. Introduction

Core excitation and de-excitation spectroscopies of gaseous atoms and molecules benefit significantly from the developments of third-generation synchrotron radiation (SR) sources and soft X-ray monochromators.[1] It is now possible to perform core excitations with a monochromator bandwidth smaller than the lifetime width of the core-excited states. In the case of atomic X-ray absorption (excitation) spectra, the apparent widths of the lines often decrease with an increase in the resolution and higher Rydberg members emerge. In the case of molecular X-ray excitation spectra, not only Rydberg series but also vibrational structures can be resolved well. A significant progress of core excitation spectroscopy was in fact achieved at second-generation SR sources some ten years ago with the development of high-resolution soft X-ray monochromators (see, for example, refs. 2–5). A renewal of interest in this field was invoked by the unprecedented resolution achieved at the third-generation SR sources.[6–14]

A narrow-band excitation provides us with large benefits also for de-excitation spectroscopy, or to be more specific, resonant Auger electron spectroscopy. If the monochromator bandwidth is smaller than the lifetime width of the core-excited state, the spectral widths of the resonant Auger emission lines are not determined by the lifetime width of the core-excited state but is determined by the convolution of the monochromator bandwidth, the bandwidth of the electron energy analyzer and the Doppler width due to thermal motion of the sample gases.[15] This line-narrowing effect, often called *resonant Auger Raman* effect, can be used for spectroscopic investigations for the Auger final ionic states. The activities in this field at the second-generation light sources were well described in a review article.[16] Progress in this field at the third-generation light sources can be seen in, for example, refs. 17–28. Partial cross sections can also be extracted from the de-excitation spectra recorded as a function of photon energy, since the monochromatic soft X-rays at the third-generation light sources are intense enough to record the photoemission spectra even in the inter-resonance regions. Such partial cross section measurements turned out to reveal interference effects between the direct and resonant channels[29–31] as well as among the resonant channels.[10,32]

If de-excitation spectroscopy is applied to molecules, it becomes a powerful tool for investigating molecular potential energy surfaces of the core-excited states and Auger final ionic states as well as nuclear dynamics along these potential energy surfaces. The lifetimes of the core-excited states for light atoms such as B, C, N, O, and F are on the order of 10^{-15} s. Within this time scale, however, the nuclear motion of the molecule proceeds in the core-excited state and this nuclear motion can be reflected in the resonant Auger electron spectrum. Activities in this field at the second-generation light sources were well described in a review article.[33] A number of papers on molecular resonant Auger emission study with the third-generation light sources have already been published; these studies have successfully probed potential energy surfaces and nuclear dynamics. See, for example, refs. 34–50.

The aim of this article is to review the current status of core excitation and de-excitation spectroscopic studies of atoms and molecules. The related subjects are widely spread as briefly discussed above, although the works listed above are a subset of the entire range of activities, and thus it is beyond the scope of this article to review all the activities. Instead of trying to cover most of the activities, this article provides a description of only some specific studies on limited samples, Ne,[10,18,21–24,26,27] CO,[50] H_2O,[12,47,48] and CF_4,[41,51] studied at beam line 27SU[52,53] of SPring-8 in Japan, one of the typical third-generation soft X-ray beam lines devoted to gas-phase atomic and molecular science.[1] It is hoped that this small subset of case studies will reveal the current status of atomic and molecular core spectroscopies that use monochromatic soft X-rays with a very narrow bandwidth available at the third-generation light sources.

2. Ne 1s excitation/de-excitation

2.1 Total ion yield spectrum

The ground state neon atom has the electronic configuration $1s^2 2s^2 2p^6$. The total ion yield spectrum in the region of the $1s \rightarrow np$ Rydberg excitation, recorded with a 4π-sr ion detector is shown in Fig. 1,[10] together with a least-squares fit (see below). The spectral dependence of the total ion yield is equivalent to that of the photoabsorption cross section. The monochromator bandwidth is ~66 meV, as
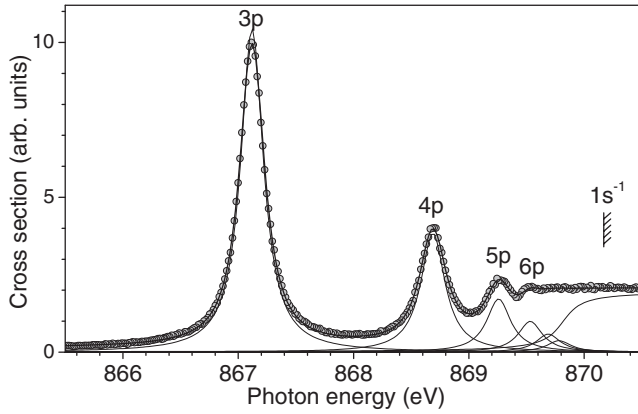
*E-mail: ueda@tagen.tohoku.ac.jp

Fig. 1. Circles: measured total cross section for photoionization of Ne in 1s excitation region. Thick line: least-squares fit, convoluted with Gaussian function with FWHM fixed to 66 meV. Thin lines: contributions from individual resonances, before convolution. From ref. 10.

estimated from Xe 5p photoelectron spectra. The photon energy scale in Fig. 1 is calibrated using the energies of the 1s3p and 1s4p resonances reported in ref. 6. This spectrum is similar to the one presented in ref. 6, but the resolution in Fig. 1 is slightly higher and thus the 1s6p resonance is partially resolved.

Photoabsorption cross sections in the core excitation regions are usually analyzed with the following expression:[54]

$$\sigma = \sigma_{\mathrm{dir}} + \sum_m \frac{\sigma_m}{1 + \epsilon_m^2} + \sigma_{1s}, \qquad (1)$$

where m labels the resonances and the parameters $\epsilon_m = (h\nu - E_m)/(\Gamma_m/2)$ are the distances of the photon energy $h\nu$ from the resonant energies E_m measured in terms of half lifetime widths (HWHM) $\Gamma_m/2$. σ_m and σ_{dir} are the cross sections for resonant and direct ionization, respectively. $\Gamma_m/2$, σ_m, and σ_{dir} are considered constant in the energy interval of interest. The term σ_{1s} in eq. (1) represents the 1s ionization cross section:

$$\sigma_{1s} \propto \frac{1}{2} + \frac{1}{\pi} \arctan[2(h\nu - E_{1s})/\Gamma]. \qquad (2)$$

In the fitting routine, eq. (1) is convoluted with a Gaussian function with fixed FWHM of 66 meV in order to simulate the photon bandwidth. The fit extracts the line strengths, Lorentzian widths and energies of the resonances. Although 1s7p and 1s8p cannot be resolved, they are also included in the fit, in order to reach an overall better agreement between the fit and the measurement. Contributions from higher members are included in σ_{1s}. Some parameters are fixed using quantum defect methods.[55] Namely, the energies of the 1s6p–1s8p resonances are fixed to the values extrapolated from the 1s3p–1s5p resonances, whereas the line strengths of 1s7p and 1s8p relative to the line strength of 1s6p are fixed. The widths are assumed to be the same for the resonances 1s4p–1s8p. The widths for these high-n members, however, turn out to be the same as that of 1s3p via fitting within the experimental uncertainties. The value thus obtained for the lifetime width, $\Gamma_{3p} = 240 \pm 10$ meV, is slightly lower than the calculated one in ref. 6, $\Gamma_{3p} = 258$ meV.

We note here, for later discussion, the relation between the Lorentzian function included in eq. (1):

$$\sigma_L = \frac{\sigma}{1 + \epsilon^2} \qquad (3)$$

and Fano's resonance formula:[56]

$$\sigma_F = \sigma_a \frac{(q + \epsilon)^2}{1 + \epsilon^2} + \sigma_b, \qquad (4)$$

where q is Fano's profile index, σ_a and σ_b are the cross sections for excitation to the continuum that does and does not interact with the discrete isolated resonance, respectively. The Lorentzian function is the limit $q \to +\infty$, with $\sigma_a q^2$ being still finite ($\sigma_a q^2 = \sigma$) in Fano's resonant function, eq. (4). Although the interaction of the resonances with the continuum channels may not be negligible, the Lorentzian functions in eq. (1) are still good approximations for the resonant profiles in the total cross section, as can be seen in Fig. 1. Later we will discuss this point further.

2.2 Resonant Auger spectrum after 1s → 3p excitation

When one tunes the photon energy to the 1s3p resonance in Fig. 1 and detects the electron emission from the neon atom, then one can see the so-called resonant Auger spectrum. The resonant Auger transitions can be classified into two groups: participator Auger transitions and spectator Auger transitions. In the participator Auger transitions, the electron promoted to the unoccupied orbital (e.g., 3p in the case of neon) participates in the Auger transitions, whereas the promoted electron (e.g., the 3p electron of neon) behaves as a spectator in the spectator Auger transitions.

Figure 2 shows a portion of the electron spectra of the spectator Auger transitions.[18] The spectra were recorded using a state-of-the-art electron spectroscopy apparatus, whose heart was a 200-mm-radius hemispherical electron
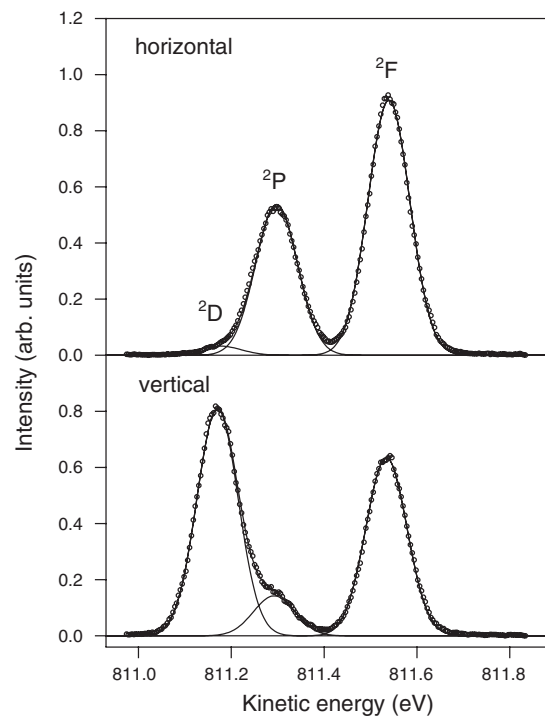

Fig. 2. Part of electron spectra of resonant Auger transitions from Ne 1s3p state to final Ne$^+$ 2p^4(^{1}D$_2$)3p ^{2}D, ^{2}P, and ^{2}F states, recorded at photon energy of 867.12 eV with horizontal (upper) and vertical (lower) polarizations. From ref. 18.
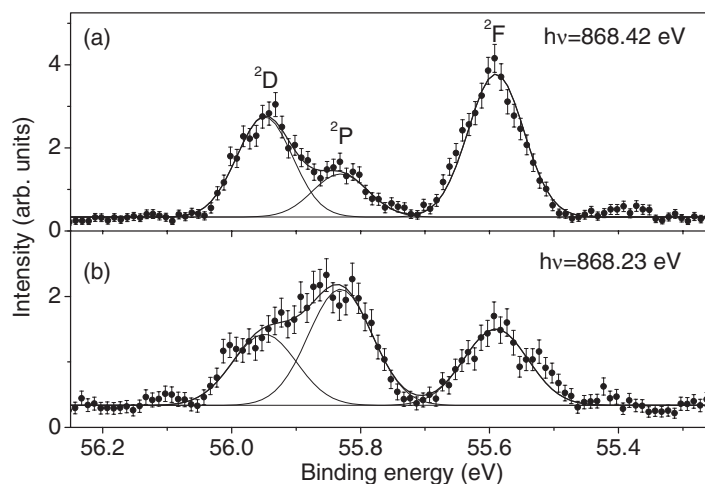
Fig. 3.   Angle-integrated electron spectra measured at photon energies of (a) 868.42 and (b) 868.23 eV, together with fit by Gaussian profiles. From ref. 10.

analyzer (Gammadata-Scienta SES-2002). The lens axis of the analyzer was horizontal and perpendicular to the photon beam axis.[57] A sample gas was introduced into the gas cell attached to the lens and was differentially pumped. The excitation photon energy was 867.12 eV, i.e., the 1s3p resonance energy. The directions of the light polarization were horizontal and vertical for the upper and lower spectra, respectively, in Fig. 2. The direction of the polarization could be switched by just changing the gap of the figure-8 undulator,[58] without changing any beam line optics. The analyzer was operated at a pass energy of 20 eV, resulting in an analyzer bandwidth of ∼13 meV.

The three lines in Fig. 2 arise from the transitions from the Ne 1s3p state to the final Ne$^+$ 2p^4(^{1}D$_2$)3p ^{2}P, ^{2}D, and ^{2}F states. The resonant Auger spectra were observed previously at moderate resolutions without resolving these multiplet structures.[17,32,59,60] The Ne$^+$ 2p^4(^{1}D$_2$)3p ^{2}P, ^{2}D, and ^{2}F states do not decay further via electron emission. The energy separations between the doublet components are negligible according to the theoretical calculations employing the multiconfiguration Dirac–Fock (MCDF) approach.[18]

The spectra in Fig. 2 were well fitted to the three Gaussian profiles of ∼105 meV FWHM as shown in Fig. 2. A separate measurement confirms that a line profile of each of these Auger lines coincides with that of the Ne 2s and 2p photolines within the experimental uncertainties. Gaussian profiles were chosen because in the electron spectra the broadening caused by instrumental and Doppler effects was much larger than the lifetime width of the Auger final states. The experimental width of ∼105 meV is indeed a convolution of the three Gaussian components; the monochromator bandwidth of ∼66 meV, the analyzer bandwidth of ∼13 meV, and the Doppler width of 79 meV due to the thermal motion of the Ne atoms.

The branching ratio for the 2p^4(^{1}D$_2$)3p ^{2}P, ^{2}D, and ^{2}F final states as well as the anisotropy parameters β were extracted from several spectra similar to those in Fig. 2. The branching ratio is 0.18 ± 0.01 : 0.35 ± 0.02 : 0.47 ± 0.02 for ^{2}P : ^{2}D : ^{2}F and nearly the same as the statistical ratio 0.2 : 0.33 : 0.47 (= 3 : 5 : 7). The β values are 0.98 ± 0.07, −0.95 ± 0.06, and 0.27 ± 0.05 for ^{2}P, ^{2}D, and ^{2}F, respectively. These values are in good agreement with the

predicted values 1.0, −1.0, and 0.286 for ^{2}P, ^{2}D, and ^{2}F, respectively, based on the spectator model within the LSJ-coupling scheme where the electron wave is restricted to the d wave.[61,62]

2.3 Interference effects in resonant photoemission

De Fanis *et al.* measured electron emission to the Ne$^+$ 2p^4(^{1}D$_2$)3p ^{2}P, ^{2}D, and ^{2}F states also at various photon energies in the 1s excitation region, with the monochromator bandwidth of ∼66 meV and analyzer bandwidth of ∼33 meV.[10] The analyzer bandwidth was set to a larger value than that in Fig. 2. The angle-integrated spectra, $I(0°) + 2 \times I(90°)$, were obtained from the 0°- and 90°-spectra, i.e., $I(0°)$ and $I(90°)$, respectively, after correction for photon flux intensity and degrees of linear polarization (see ref. 20 for a general procedure). At photon energies where the electron count rates were low, the acquisition time was increased, so that measurements at all photon energies had enough statistics to extract the line strengths with sufficiently small uncertainties.

Figure 3 shows two examples of angle-integrated electron spectra recorded at two photon energies close to the energy for the minimum of the cross section between the 3p and 4p resonances. The error bars contain the statistical contributions as propagated from the number of counts in the original spectra. From the spectra similar to Fig. 3, the line strength of each component was extracted as a function of photon energy, by a least-squares fit with Gaussian profiles. In the fit for each electron spectrum, the separations between the states were fixed at the values obtained at the peak of the 3p resonance[18] (see Fig. 2). The partial cross sections thus measured are displayed in Fig. 4(a).[10] All the resonances show nearly symmetric profiles in every partial cross section. Close inspections, however, reveal that the resonance exhibits slightly different asymmetric profiles for different partial cross sections. The relative branching ratios obtained from the measured partial cross sections exhibit dramatic oscillations typical of interference effects, as can be seen in Fig. 4(b).

Using the model of Kabachnik and Sazhina[63] (see also ref. 64), the amplitude for each specific channel α in the region of one isolated resonance is written as follows:
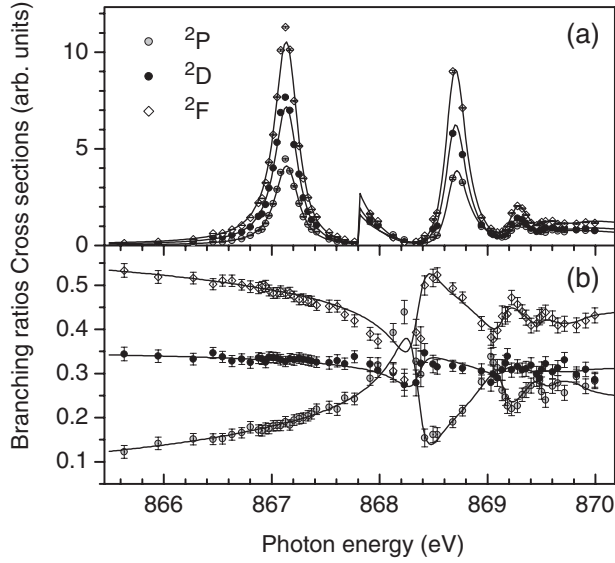
Fig. 4. (a) Measurements of partial cross sections to $2p^4(^1D_2)3p$, together with fit of individual components. (b) Branching ratios extracted from the measured electron spectra (points), and from corresponding fit (lines). From ref. 10.

$$A_\alpha = d_\alpha + \mathcal{D}_\alpha \frac{q + \epsilon}{i + \epsilon}, \qquad (5)$$

where d_α and $\mathcal{D}_\alpha$ represent the amplitudes of the direct and resonant processes, respectively, and i is an imaginary unit. Equation (5) can be generalized to the case of more than one resonance in the following way:

$$A_\alpha = d_\alpha + \sum_m \mathcal{D}_{m\alpha} \frac{q_m + \epsilon_m}{i + \epsilon_m}. \qquad (6)$$

Note that q in eq. (5) is the same as in eq. (4). Following the result that the resonance profiles in the total cross section σ are symmetric (i.e., $q_m \to +\infty$ and $D_{m\alpha} = q_m \mathcal{D}_{m\alpha}$, where $D_{m\alpha}$ is related to the dipole moment of the resonance excitation), eq. (6) can be replaced by

$$A_\alpha = d_\alpha + \sum_m \frac{D_{m\alpha}}{i + \epsilon_m}. \qquad (7)$$

In this model, each channel α is defined by the final ionic state j and by the angular momentum l of the outgoing electron, $\alpha \equiv (j, l)$, as in ref. 63. We assume the LSJ coupling scheme. Then, each partial cross section σ_j corresponds to the incoherent sum of the two different photoelectron channels $l = 0, 2$. Thus, each partial cross section is parameterized as follows:

$$\sigma_j = A_j + B_j \sum_m \frac{R_m^2}{1 + \epsilon_m^2} + \sigma_{dir-res,j} + \sigma_{res-res,j} + \sigma_{1s,j}, \quad (8)$$

with R_m normalized so that R_{3p} is unity. The direct–resonant $\sigma_{dir-res,j}$ and resonant–resonant $\sigma_{res-res,j}$ interference terms are given as follows:

$$\sigma_{dir-res,j} = 2C_j \sum_m \frac{R_m \epsilon_m}{1 + \epsilon_m^2}, \qquad (9)$$

and

$$\sigma_{res-res,j} = 2B_j \sum_{m<n} \frac{R_m R_n (1 + \epsilon_m \epsilon_n)}{(1 + \epsilon_m^2)(1 + \epsilon_n^2)}. \qquad (10)$$

A_j, B_j, and C_j are defined as

$$A_j = \sum_{l=0,2} d_{j,l}^2, \qquad (11)$$

$$B_j R_m R_n = \sum_{l=0,2} D_{m,j,l} D_{n,j,l}, \qquad (12)$$

$$C_j R_m = \sum_{l=0,2} d_{j,l} D_{n,j,l}. \qquad (13)$$

$\sigma_{1s,j}$ described by the same analytic form as eq. (2) expresses the contributions from high $1snp$ ($n \geq 9$) members as well as from the 1s ionization.

The electron spectra recorded at the peak of each resonance show almost the same branching ratios, close to the statistical ratios expected within the LSJ-coupling scheme: $B_{^2P} : B_{^2D} : B_{^2F} = 3 : 5 : 7$. We thus assume that different resonances have the same branching ratios over different final states. This makes B_j well defined in eq. (12). In general, from eqs. (11)–(13), A_j, B_j, C_j are constrained to fulfill the triangular inequality $A_j B_j \geq C_j^2$. However, by using the spectator model within the LSJ-coupling scheme, the photoelectron wave is restricted to $l = 2$ and then $A_j B_j = C_j^2$.

The partial cross sections in Fig. 4(a) are fitted simultaneously using the model described above. In the fitting, the profiles given by eq. (8) are broadened by convolution with a Gaussian distribution with FWHM fixed to 66 meV to simulate the monochromator bandwidth. As can be seen in Fig. 4(a), the fit reproduces well the measurements. The continuous lines superimposed on the measured branching ratios in Fig. 4(b) are not the results of an additional fit, but the branching ratios calculated from the three simultaneous fits for the partial cross sections in Fig. 4(a). The agreement between the continuous lines and the experimental points is reasonable.

Let us consider how the interference plays a role in describing the oscillations in the branching ratios. If the direct ionization process is absent for all the channels, the branching ratios to the Ne$^+$ $2p^4(^1D_2)3p$ ^2P, ^2D, and ^2F states become constant in the present model. If the direct process is present, then the energy for the minimum of the cross section varies depending on the ratio between A_j and B_j. Thus, it is clear that the direct–resonant interference term is essential in describing the oscillations of the branching ratios. On the other hand, if the resonant–resonant interference term were switched off, each partial cross section would not approach zero any more in the inter-resonance regions and thus the amplitudes of the oscillations would be significantly suppressed. Indeed, attempts to fit the partial cross sections with the incoherent sum of the the Fano profile given by eq. (4) fail to reproduce the large oscillations of the branching ratios in the inter-resonance regions. This is a clear indication that the $\sigma_{res-res}$ terms are important, i.e., the resonances are not isolated., as a natural consequence of the requirement by quantum mechanics, where the amplitudes, not the squared probability, should be coherently summed up.

2.4 Doppler-free resonant Auger spectroscopy

We note that the spectral widths of the spectator Auger spectra in Fig. 2 are dominated by the contributions of
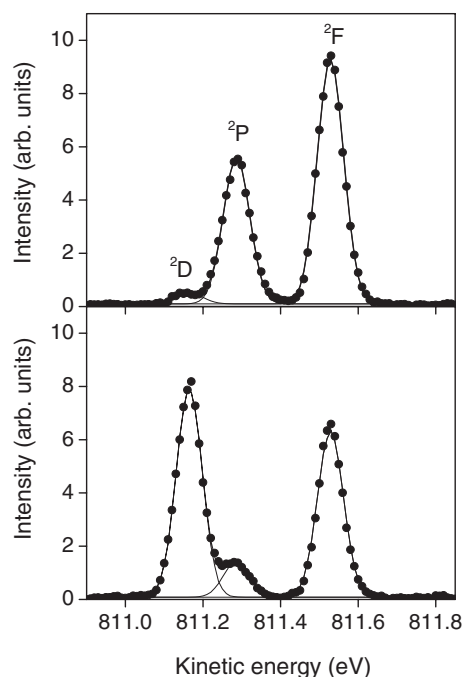
Fig. 5. Part of electron spectra of resonant Auger transitions of Ne similar to Fig. 2 but under "Doppler-free" conditions obtained using molecular beam device. From ref. 65.

Doppler broadening. The Doppler energy shift is given by the scaler product of the electron momentum and the momentum of the emitter. Thus, if one uses a well-collimated molecular beam, whose velocity component perpendicular to the beam direction is negligible, as a target and observes the electron emission in the direction of perpendicular to the molecular beam, then one can suppress the Doppler broadening. Figure 5 presents the same portion of the electron spectra of Ne as in Fig. 2.[65] Here, we employed the *Doppler-free* molecular beam instead of the gas cell. The beam device has an orifice of $1 \times 8\,\text{mm}^2$, covered by a 1-mm-thick microchannel plate. A multi-channel array permits a much higher target pressure than a single-tube device. The inlet pressure of an effusive beam

source is limited roughly to 1 Torr, i.e., the level where the mean free path related to intermolecular collisions is smaller than the channel diameter. The analyzer was operated at a pass energy of 50 eV resulting in an analyzer bandwidth of ~33 meV. The spectra are well fitted to the three Gaussian profiles of 74 meV FWHM as shown in Fig. 5. The experimental width of 74 meV corresponds to a convolution of the analyzer bandwidth ~33 meV and the monochromator bandwidth ~66 meV.

The left panel of Fig. 6 shows a portion of the electron spectra corresponding to the transitions to Ne$^+$ 2s2p^5(^{1}P)3p via the Ne 1s → 3p excitation at a photon energy of 867.12 eV, whereas the right panel shows a portion of the electron spectra corresponding to the transitions to Ne$^+$ 2s2p^5(^{3}P)3p via the Ne 1s → 3p excitation.[21,22] The spectra were recorded using the Doppler-free molecular beam. In the left panel, two lines, lines 1 and 2, are clearly resolved in the 90° spectrum (perpendicular polarization). In the 0° spectrum (horizontal polarization), line 1 becomes weak and further-more we notice one more broad line, line 3, at the foot of line 2. In the right panel, lines 5 and 6 are resolved in the 90° spectrum, whereas line 5 is suppressed and line 4 appears in the 0° spectrum. We note also that the widths are different for different lines. This is because the spectator Auger final states Ne$^+$ 2s2p^5(^{1}P, ^{3}P)3p are subject to second-step Auger decay and thus the different widths reflect the different lifetimes of the decaying states.

The spectra similar to the ones in Fig. 6 were recorded sequentially and repeatedly together with the spectra for the transitions to the Ne$^+$ 2p^4(^{1}D)3p ^{2}P, ^{2}D, and ^{2}F states; the experimental conditions were slightly different from those in Fig. 5. The instrumental function (described by the Gaussian components) was extracted from the spectrum for the transitions to the Ne$^+$ 2p^4(^{1}D)3p ^{2}P, ^{2}D, and ^{2}F states. To carry out the fitting to the spectra in Fig. 6, each profile of the lines was described by a convolution of the Lorentzian function and the known instrumental function (Gaussian functions). The Lorentzian width of each line corresponds to the lifetime broadening of the corresponding spectator Auger final state and was regarded as a fitting parameter: the width
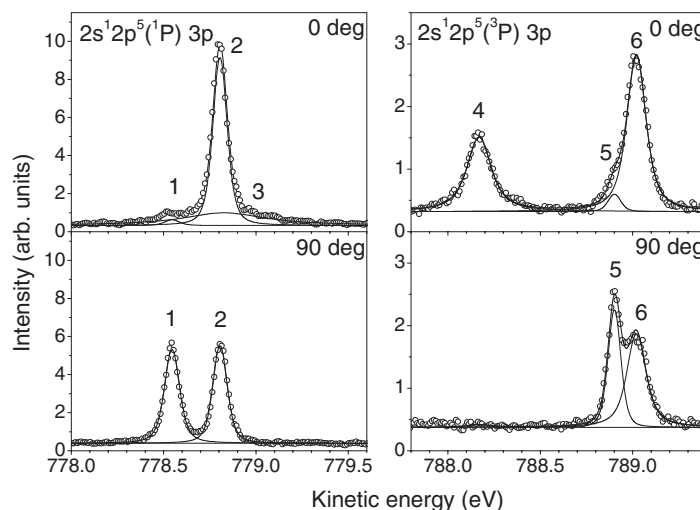

Fig. 6. Part of electron spectra of resonant Auger transitions to Ne$^+$ 2s2p^5(^{1}P)3p ^{2}P, ^{2}D, and ^{2}S states (lines 1, 2, and 3, respectively) and to Ne$^+$ 2s2p^5(^{3}P)3p ^{2}S, ^{2}P, and ^{2}D states (lines 4, 5, and 6, respectively) via Ne 1s3p state at photon energy of 867.12 eV with horizontal (upper) and vertical (lower) polarizations. The thick lines are the results of the fit, and the thin lines are the individual components. From ref. 22.

Table I. Measured and calculated transition energies, anisotropy parameters β, and branching ratios (for each parent state) for resonant Auger decay to Ne$^+$ 2s2p^5(^{1}P,^{3}P) 3p ^{2}S, ^{2}P, and ^{2}D states.[21] The uncertainties of the measured transition energies are ∼0.02 eV in the relative scale and ∼0.1 eV in the absolute scale.

Final state	E_k (eV)		β		Branching ratio	
	Expt.	Theor.	Expt.	Theor.	Expt.	Theor.
(^{1}P) 3p ^{2}P	778.55	776.40	-0.94 ± 0.06	-0.996	0.35 ± 0.02	0.340
(^{1}P) 3p ^{2}D	778.81	776.66	0.15 ± 0.06	0.200	0.54 ± 0.02	0.561
(^{1}P) 3p ^{2}S	778.83	776.43	$2.0^{+0.0}_{-0.2}$	2.000	0.12 ± 0.02	0.099
(^{3}P) 3p ^{2}S	788.17	786.51	1.8 ± 0.2	1.998	0.15 ± 0.02	0.153
(^{3}P) 3p ^{2}P	788.90	787.52	-0.8 ± 0.1	-0.928	0.28 ± 0.02	0.324
(^{3}P) 3p ^{2}D	789.02	787.64	0.15 ± 0.05	0.156	0.57 ± 0.02	0.523

was constrained to be the same for both 0° and 90° spectra. The details of the fitting procedure can be seen in ref. 21.

In Table I, values of transition energies, β, and branching ratios obtained from the fitting are compared with the theoretical calculations using the MCDF approach.[21] Comparing the measured values with the calculated ones averaged over the unresolved final J states for each multiplet, we attribute lines 1, 2, and 3 to the transitions to the Ne$^+$ 2s2p^5(^{1}P)3p ^{2}P, ^{2}D, and ^{2}S states, respectively, and lines 4, 5, and 6 to the transitions to the Ne$^+$ 2s2p^5(^{3}P)3p ^{2}S, ^{2}P, and ^{2}D states. The measurements are in reasonable agreement with the calculations for both the β values and the branching ratios.

The lifetime widths of the spectator Auger final states, which can be extracted as the Lorentzian widths from the fitting, are presented in Table II, together with the existing theoretical calculations and previous measurements. The results for the Ne$^+$ 2s2p^5(^{1,3}P)3p ^{2}S line agree reasonably well with those extracted from the early measurements for the satellite structure of Ne photoionization.[66] We first focus on the widths of the 2s2p^5(^{1}P)3p states. Calculations by Armen and Larkins obtained in a single-configuration Hartree–Fock approximation[67] semiquantitatively reproduce the experimental observation that the lifetime width of the Ne$^+$ 2s2p^5(^{1}P)3p ^{2}S state is one order of magnitude shorter than Ne$^+$ 2s2p^5(^{1}P)3p ^{2}P and 2s2p^5(^{1}P)3p ^{2}D. An analysis of the contributions to the width of the Ne$^+$ 2s2p^5(^{1}P)3p states from the inner-valence participator Auger transitions to the Ne^{2+} 2s^{2}2p^4 final states and the intermultiplet Auger transitions to the Ne^{2+} 2s^{1}2p^5 final states shows that the former is dominant for the ^{2}P and ^{2}D lines while the latter determines the broad width of the ^{2}S line.[67] Let us turn to Ne$^+$ 2s2p^5(^{3}P)3p states. Note that there are no more intermultiplet Auger transitions from these states. Calcula-

tions by Armen and Larkins[67] fail to reproduce the experimental width of the Ne$^+$ 2s2p^5(^{3}P)3p ^{2}S state, whereas the elaborate theoretical calculations by Sinanis et al.[68] successfully reproduce the experimental width. This transition is very sensitive to electron correlations and can be well described only if the correlations are fully taken into account. The widths of other multiplets ^{2}P and ^{2}D are smaller than 2s2p^5(^{1}P)3p ^{2}S. The measured values are rather close to the predictions of Armen and Larkins.[67]

2.5 Second-step Auger spectrum via 1s → 3p excitation

One can also measure the second-step Auger spectrum which arises from the decay of the Ne$^+$ 2s2p^5(^{1,3}P) 3p $^{2S+1}$L states. Figure 7 shows the part of the electron spectra measured at 0° (upper panel) and 90° (lower panel) in the electron kinetic energy interval 10–33 eV for the photon energy of 867.12 eV corresponding to the Ne 1s3p resonance. In many cases, the multiplet structure of each numbered line was resolved.

Table II. Measured and calculated widths in meV for Ne$^+$ 2s 2p^5(^{1}P, ^{3}P) 3p ^{2}S, ^{2}P, and ^{2}D states.

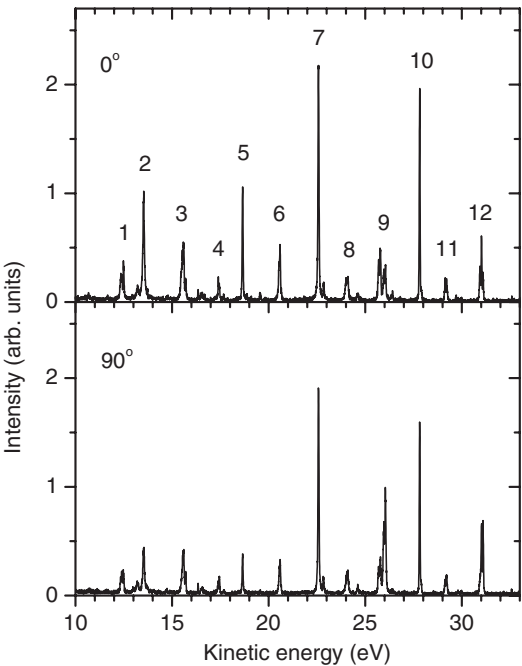| Final state	Experiment		Theory		
	Doppler free[21]	Second step[24]	ref. 66	ref. 67	ref. 68
(^{1}P) 3p ^{2}P	42 ± 5	37 ± 2		20.7	
(^{1}P) 3p ^{2}D	34 ± 5	34 ± 3		40.2	
(^{1}P) 3p ^{2}S	530 ± 50		410 ± 50	687	510
(^{3}P) 3p ^{2}S	120 ± 10	111 ± 10	110 ± 40	18.8	122
(^{3}P) 3p ^{2}P	19 ± 5	$24^{a)}$		10.3	
(^{3}P) 3p ^{2}D	80 ± 10	$18^{a)}$		62.3	

a) Errors could not be estimated for unresolved lines.

Fig. 7. Low-energy part of electron spectra generated at resonant excitation of Ne 1s3p state by photons with energy of 867.12 eV with horizontal (upper) and vertical (lower) linear polarizations. The numbers indicate the groups of lines corresponding to the transitions between states with particular configurations. From ref. 24.
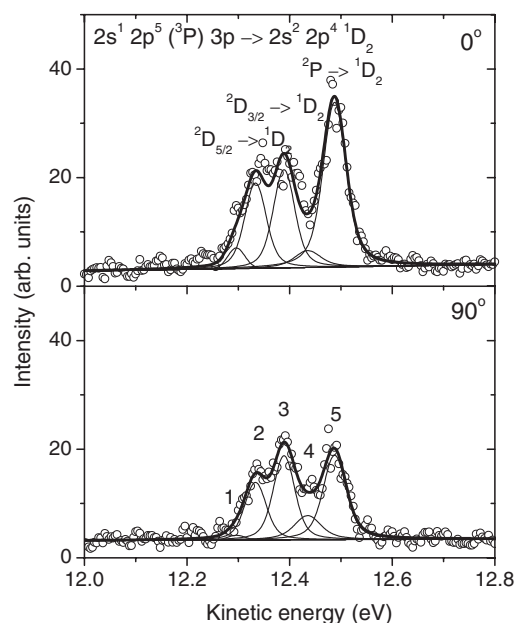
Fig. 8. Part of electron spectra (circles) of second-step Auger transitions corresponding to peak 1 in Fig. 7. The lines are assigned to the $2s^12p^5(^3P)3p \to 2s^22p^4\ ^1D_2$ transitions. The thick solid line shows the results of the fit (see text); thin lines show contributions of particular transitions between multiplets indicated in the figure. Upper and lower panels correspond to horizontal and vertical photon polarization, respectively. From ref. 24.

A group of lines labeled peak 1 in Fig. 7 is enlarged and presented in Fig. 8. These lines are attributed to the Ne$^+$ $2s2p^5(^3P)3p \to$ Ne^{2+} $2s^22p^4\ ^1D_2$ transitions.[59] Three components, lines 2, 3, and 5, can be recognized and assigned to $^2D_{5/2} \to\ ^1D_2$, $^2D_{3/2} \to\ ^1D_2$, and $^2P \to\ ^1D_2$ transitions, respectively. These assignments are based on the relative energies calculated by the MCDF approach.[24] The measured relative intensities are 0.54, 0.72, and 1 for these three lines, whereas the calculated relative intensities are 1.44, 1.27, and 1, respectively. The β values of these three lines (not listed here) do not agree well with the calculated values. We note that the initial levels for this group are strongly mixed and that there are several other weak transitions in this energy interval. In this situation, the theoretical results for β are very sensitive to the admixture of other configurations. A weaker line 1, which is seen as a shoulder on the left side of line 2, is probably the transition $^4P_{5/2} \to\ ^1D_2$, which is comparatively strong in the calculations. There is an additional unassigned peak 4 between lines 3 and 5.

We note here that the initial states of these second-step Auger transitions are the final states of the first-step Auger transitions shown in the right panel of Fig. 6. The kinetic energies of the second-step Auger electrons are lower, by more than one order of magnitude, than those of the first-step resonant Auger electrons and thus the Doppler broadening is negligible (a few meV) even when one uses the samples in the gas cell at room temperature. The width of the second-step Auger line depends on the electron analyzer bandwidth but is independent of the photon bandwidth. The observed width depends also on lifetimes of the initial and final states of the second-step Auger decay. In the present case, the lifetime broadening of the final state is negligible. Thus, one

can extract the lifetime widths of the initial states of the second-step Auger decay, i.e., the final state of the first-step resonant Auger decay. The lifetime widths extracted from the second-step Auger decay are also included in Table II. The agreements are in general good. A discrepancy appears only for the line of $2s2p^5(^3P)3p\ ^2D$, where the multiplet structure was resolved only in the second-step Auger spectrum as seen in Fig. 8.

2.6 Evolution of spectator Auger to normal Auger decay

Thus far, we have focused on the Ne $1s \to 3p$ excitation. Here, we consider the Ne 1s excitation near the ionization threshold.[26,27]

When the Ne atom is photoionized above the 1s threshold, the Ne 1s photoelectron is emitted and then the Auger electron emission takes place, replacing one 1s hole with two valence holes. This type of Auger transition is called "normal" Auger decay, in contrast to "spectator" Auger decay based on resonant excitation. The strongest normal Auger line in Ne arises from the transition between the 1s singly ionized state and the Ne^{2+} $2p^4\ ^1D_2$ state. If the photon energy is very close to the Ne 1s ionization threshold, the emitted photoelectron is still close to the ion at the moment when Auger decay occurs. Then, the postcollision interaction (PCI) among the two electrons and the ion takes place. Due to PCI, the Auger electron is accelerated while the photoelectron is retarded and sometimes recaptured by the ion into one of its Rydberg orbitals.[69,70]

The top panel of Fig. 9 displays a part of the Ne Auger spectrum recorded at an excitation energy (excess energy) of $E_{exc} = 0.6\,\mathrm{eV}$ above the 1s ionization threshold. The spectrum arises from the Auger transition to Ne^{2+} $2p^4\ ^1D_2$. The vertical dotted line shows the nominal Auger energy E_A, i.e., the energy of the normal Auger line when the excitation energy is sufficiently high. The observed Auger line has a typical PCI-distorted line shape and shifts upwards in energy with respective to E_A, as is well known from many previous studies.[71] The vertical solid line shows the difference between photon energy and Ne^{2+} $2p^4\ ^1D_2$ double ionization potential (if one refers to the bottom x-axis, or the excess energy if one refers to the top x-axis). The part of the spectrum on the high-kinetic-energy side of this line pertains to recapture processes. The spectrum of this part exhibits the sharp Auger lines arising from the transitions to the Ne$^+$ $2p^4(^1D_2)np$ states, where the np Rydberg levels are populated by the recaptured photoelectrons. Gray boxes are drawn following the recipe of the quantum-defect theory,[55] taking into account the density of the final states. In this way, a smooth continuation of the normal Auger part of the spectrum (the low-kinetic-energy part of the vertical solid line) into the region below the threshold (the high-kinetic-energy part of the vertical solid line) can be visualized.

The observed spectrum is compared with the numerical implementation of the semiclassical theory by Russek and Mehlhorn.[72] The Auger amplitude in this *ansatz* is written as a Fourier transform of the time-dependent decay probability, the time evolution of which is modified by a time- and energy-dependent phase factor, which takes the PCI into account. The energy exchange between the slow photoelectron and the fast Auger electron is $1/\rho$, with ρ being the radius at which the Auger electron overtakes the
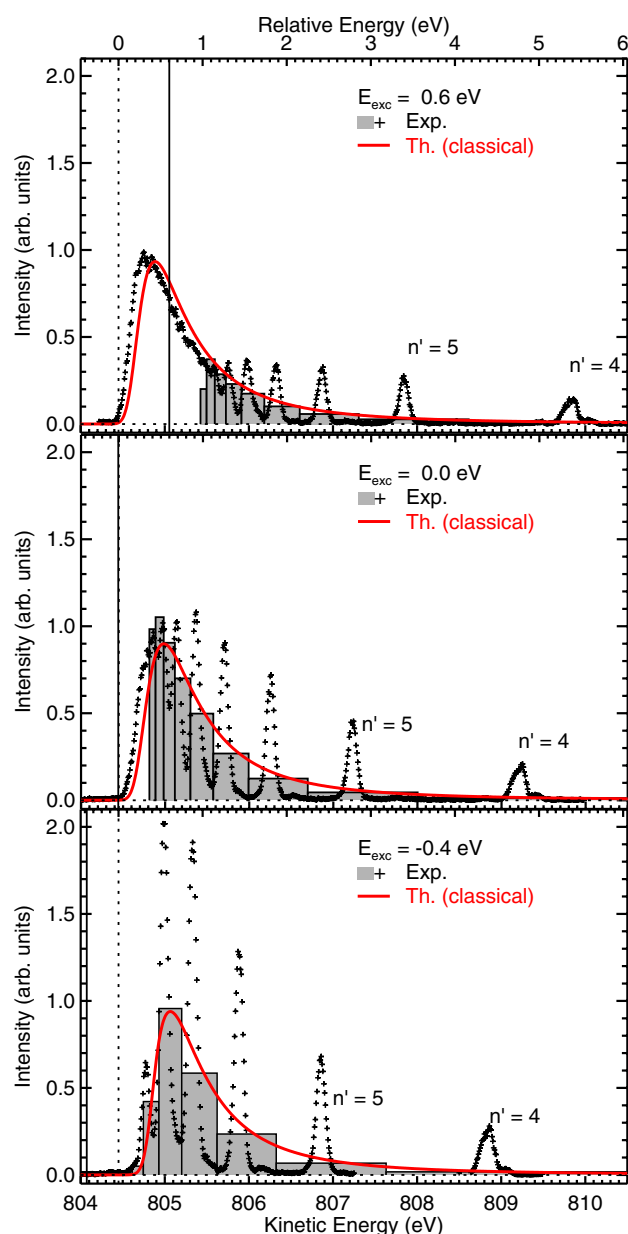
Fig. 9. (Color online) Part of Ne Auger spectrum recorded at three different excitation energies $E_{exc} = +0.6$, 0.0, and -0.4 eV, relative to N 1s ionization threshold: +, experimental data points after subtraction of constant background; solid lines, theoretical Auger electron profiles calculated using semiclassical model. Areas of the gray shaded boxes represent the experimental intensity of recapture into the $n = 3$–12 states. Normalization of the box widths and of the discrete values calculated by the quantum defect theory[55] is chosen appropriately for a continuation of the Auger part of the spectrum. From ref. 27.

photoelectron. As can be seen in the top panel of Fig. 9, the overall behavior of the observed spectrum is in very good agreement with the semiclassically calculated spectrum (solid curve), even for the region below the threshold (the high-kinetic-energy part of the vertical solid line).

The middle panel of Fig. 9 displays a part of the spectrum recorded at an excitation energy tuned to the 1s ionization threshold ($E_{exc} = 0.0$ eV). All the Auger lines lie on the high-kinetic-energy side of the the vertical line, illustrating that all the zero-kinetic-energy photoelectrons are recaptured to the Rydberg states at the moment of Auger decay, due to PCI. The bottom panel of Fig. 9 displays a part of the

spectrum recorded at $E_{exc} = -0.4$ eV (i.e., the excitation energy 0.4 eV below the Ne 1s ionization threshold). One may regard this spectrum as arising from the spectator Auger decay following the 1s excitation to the overlapping Rydberg manifold states that are unresolved because of the lifetime broadening (see Fig. 1). Comparing the three spectra in Fig. 9, one can see that the normal Auger spectrum gradually evolves to the spectator Auger spectrum as the excitation energy changes from a positive excess energy ($E_{exc} > 0$), across the threshold $E_{exc} = 0$, and to a negative excess energy $E_{exc} < 0$.

The spectra in the middle and bottom panels are also compared with the numerical implementation of the semiclassical theory by Russek and Mehlhorn.[72] Although unforeseen in the original publication,[72] one finds the implementation of this approach applicative even for the excitation below the ionization threshold ($E_{exc} < 0$). Details of this implementation have been described in ref. 26. The calculated spectra (solid curve) reproduce well the overall behavior of the observed spectra at the excitation not only above the threshold ($E_{exc} > 0$) but also below it ($E_{exc} < 0$). The continuous evolution between the normal and spectator Auger spectra well reproduced by the semiclassical calculation is a natural consequence from the fact that the Rydberg electron wavepacket ($E_{exc} < 0$) and the photo-electron wavepacket ($E_{exc} > 0$) behave in a very similar manner, within the timescale of the Auger decay, i.e., within a few femtoseconds.

2.7 Second-step Auger spectroscopy via threshold excitation

As seen in the middle panel of Fig. 9, highly excited ionic Rydberg states can be populated by a recapture process in near-threshold core photoionization. If the Auger final ionic state, say Ne$^+$ $2p^4(^1D)np$, lies above the threshold for double-ionization Ne^{2+} $2p^4$ $^3P_2$, autoionization (valence Auger decay) can occur. De Fanis et $al.$ have observed the Rydberg series of the Ne$^+$ $2p^4(^1D)np \rightarrow$ Ne^{2+} $2p^4$ ^3P intermultiplet "participator" Auger transitions by high-resolution low-energy electron spectroscopy, populating the initial Ne$^+$ Rydberg states via photoelectron recapture, and determined the spectroscopic properties of these Rydberg states.[23]

Figure 10 shows two parts of the spectrum which correspond to the lowest members of the series for the transitions Ne$^+$ $2p^4(^1D)np \rightarrow$ Ne^{2+} $2p^4$ ^3P for $n = 5$ [Fig. 10(a)] and $n = 6$ [Fig. 10(b)]. Black dots show the experimental results obtained for 0° emission with respect to the photon polarization direction. Open circles show the spectrum for the 90° emission. The lines represent the results of a least-squares fit to the spectra with Gaussian profiles of 11 meV width (FWHM). The resolution of the experiment is high enough to resolve not only the transitions to the different fine-structure levels of the final Ne^{2+} $^3P_{0,1,2}$ state, but also the multiplet structure of the excited Rydberg states.

With the help of the values calculated using the MCDF approach, the lines in the spectra shown in Fig. 10 are assigned to the transitions Ne$^+$ $2p^4(^1D)$ np $^2F \rightarrow$ Ne^{2+} $2p^4$ $^3P_{0,1,2}$ and Ne$^+$ $2p^4(^1D)$ np $^2D \rightarrow$ Ne^{2+} $2p^4$ $^3P_{0,1,2}$ ($n = 5$, 6). The measured term values T and the measured and
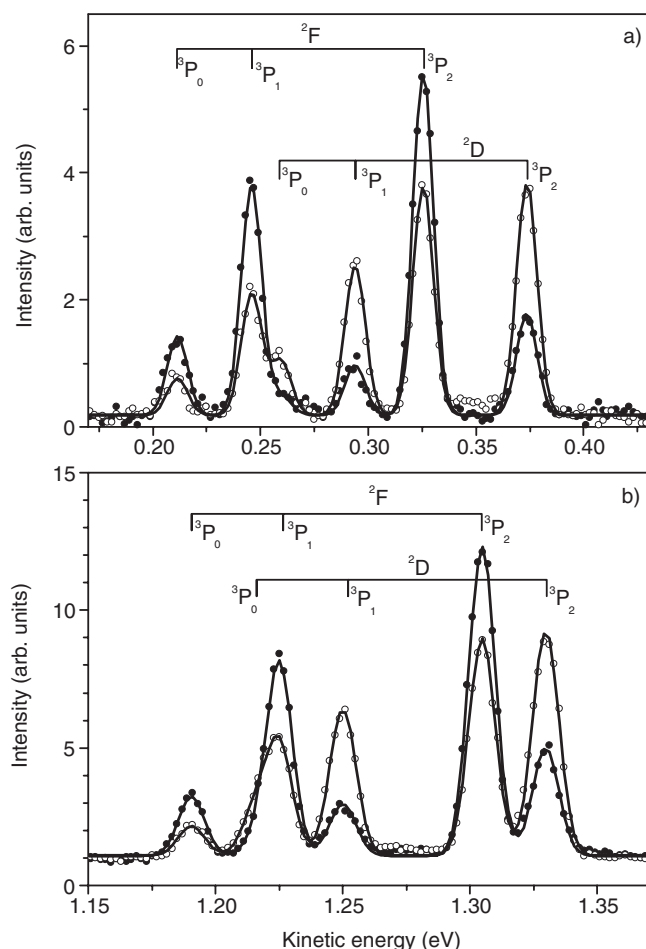
Fig. 10. Portions of low-energy-electron spectrum recorded at $0°$ (full circles) and $90°$ (open circles) relative to polarization vector. The Ne$^+$ $2p^4(^1D)np$ ^2F,^2D → Ne^{2+} $2p^4$ ^3P autoionization decays with $n = 5$, 6 are displayed in panels a) and b), respectively. The solid curves are the results of a least-squares fit described in the text. From ref. 23.

Table III. Term values, intensity ratios and angular anisotropy parameters $β$ for two lowest observed members of series Ne$^+$ $2p^4(^1D)np$ ^2F → Ne^{2+} $2p^4$ $^3P_{0,1,2}$ and Ne$^+$ $2p^4(^1D)np$ ^2D → Ne^{2+} $2p^4$ $^3P_{0,1,2}$ $(n = 5, 6)$ of intermultiplet Auger transitions.[23] Intensities have been normalized to the strongest transition for each respective n.

Initial state	Final state	T (eV)	Intensity ratio		$β$	
			Expt.	Theor.	Expt.	Theor.
$5p\,^2F$	$^3P_0$	0.212	0.19(1)	0.18	0.55(11)	0.65
$5p\,^2D$		0.260	0.16(1)	0.12	−0.56(10)	−0.70
$5p\,^2F$	$^3P_1$	0.246	0.59(1)	0.58	0.45(6)	0.55
$5p\,^2D$		0.294	0.44(1)	0.40	−0.57(6)	−0.60
$5p\,^2F$	$^3P_2$	0.326	1.00(1)	1.00	0.28(5)	0.36
$5p\,^2D$		0.374	0.71(1)	0.80	−0.46(5)	−0.34
$6p\,^2F$	$^3P_0$	1.191	0.15(1)	0.18	0.55(10)	0.65
$6p\,^2D$		1.216	0.13(1)	0.10	−0.64(10)	−0.70
$6p\,^2F$	$^3P_1$	1.225	0.55(1)	0.58	0.40(6)	0.53
$6p\,^2D$		1.250	0.46(1)	0.37	−0.55(5)	−0.57
$6p\,^2F$	$^3P_2$	1.305	1.00(1)	1.00	0.24(5)	0.37
$6p\,^2D$		1.330	0.75(1)	0.80	−0.42(5)	−0.35

Here, $1σ$ and $2σ$ denote the O 1s and C 1s core orbitals, respectively.

The best-studied example of the resonant photoemission spectra seems to be the one for CO via the C 1s → $2π$ resonance.[76–80] The lifetime width and vibrational spacing are about 0.1 and 0.3 eV, respectively, and thus the overlap is not significant. In spite of the small overlap, however, Osborne *et al.*[77] and Kukk *et al.*[78] clearly identified the influence of the resonant-resonant interference in the resonant Auger spectra. The resonant-resonant interference among the vibrational components due to lifetime broadening is often called lifetime vibrational inerference (LVI). Carravetta *et al.*, on the other hand, showed, both experimentally and theoretically, evidence for the interference effect between the direct and resonant channels.[80]

Here, we describe the investigation of interference effects in the resonant Auger spectra of CO via the O 1s → $2π$ resonance.[50] The O 1s → $2π$ absorption (total ion yield) spectrum of CO was studied by Püttner *et al.*[8] and Coreno *et al.*[81] According to their investigation, the lifetime width and the vibrational spacing are about 0.15 and 0.17 eV, respectively; thus, the overlap of the vibrational components is larger than at the C 1s → $2π$ resonance, and we can expect stronger LVI effects.

3.1 O 1s → $2π$ total ion yield spectrum

Figure 12 shows the measured total ion yield spectrum for the O 1s → $2π$ resonance in CO. The spectrum clearly shows a vibrational progression with the significantly overlapped components due to the lifetime broadening with the width $Γ$ of the order of the vibrational spacings (as shown later). As a natural consequence, a strong LVI effect is expected in the resonant Auger spectra.

We can extract the spectroscopic parameters of the core-excited state from the total ion yield spectrum in Fig. 12, assuming that the line shape of each vibrational component can be described with a Voigt profile and that the intensity distribution of these components is given by the Franck–Condon factors between the ground and core-excited states. Tanaka *et al.* performed a least-squares fitting to the
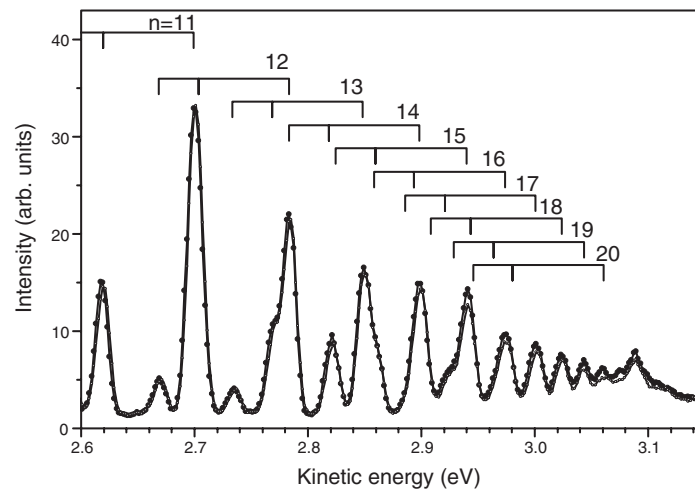
calculated relative intensities and $β$-values are shown in Table III. Good agreement confirms the assignment.

Comparing the spectra in Figs. 10(a) and 10(b), one sees that the splitting of the ^2F and ^2D initial states diminishes with an increase in n, as expected. This tendency persists for $n = 7–9$. At higher n values, however, the multiplets are already not resolved. The spectrum for higher n values is presented in Fig. 11. The strongest peaks are associated with the transitions Ne$^+$ $2p^4(^1D)np$ → Ne^{2+} $2p^4$ $^3P_2$. However, rather often, they overlap with the weaker lines corresponding to the transitions to other members of the ^3P multiplet. The series is clearly seen up to $n = 20$. From the energy positions of the lines, the quantum defects $δ$ are obtained and presented in Table IV together with the term values T. The obtained $δ$ values are constant within the experimental errors and agree well with those derived from measurements of satellite states.[75]

Many other Rydberg series have also been investigated by De Fanis *et al.*[25] and Kitajima *et al.*[28]

3. O 1s Excitation/De-excitation of CO

The ground-state electronic configuration of the CO molecule is

$$1σ^2\ 2σ^2\ 3σ^2\ 4σ^2\ 1π^4\ 5σ^2;\ 2π^0\ 6σ^0\ X\ ^1Σ^+.$$

Fig. 11.   Low-energy-electron spectrum of Ne⁺ 2p⁴(¹D)np ²F,²D → Ne²⁺ 2p⁴ ³P autoionization decay, with $n \geq 11$, recorded at 0° (full circles) and 90° (open circles) relative to polarization vector. From ref. 23.

Table IV.   Term values T and quantum defects δ of initial states for higher members of series Ne⁺ 2p⁴(¹D) np → Ne²⁺ 2p⁴(³P₂).[23] The series limit is 3.20385 eV.[73,74]

n	T (eV)	δ	n	T (eV)	δ
10	0.619	0.624(15)	16	0.230	0.60(16)
11	0.503	0.600(21)	17	0.202	0.60(08)
12	0.419	0.610(27)	18	0.180	0.60(10)
13	0.354	0.604(35)	19	0.160	0.58(11)
14	0.305	0.642(44)	20	0.143	0.49(14)
15	0.263	0.617(55)			

Table V.   Spectroscopic constants of O 1s⁻¹2π core-excited state obtained by Tanaka $et\ al.$[50] via least-squares fitting to total ion yield curve in Fig. 12, and those obtained by Püttner $et\ al.$[8] and Coreno $et\ al.$:[81] Γ, lifetime width; ω_e, vibrational frequency; $\omega_e x_e$, anharmonicity; r_e, equilibrium distance.

	Tanaka[50]	Püttner[8]	Coreno[81]
Γ (meV)	156(10)	143(5)	158(8)
ω_e (meV)	167(1)	166(1)	166(3)
$\omega_e x_e$ (meV)	1.6(1)	1.8(1)	1.7(5)
r_e (Å)	1.288(1)	1.291(1)	1.292(1)

literature values of the Morse parameters (vibrational frequency ω_e, anharmonicity $\omega_e x_e$, and equilibrium distance r_e) were used for the ground state,[82] whereas for the core-excited state, ω_e, $\omega_e x_e$, and r_e were treated as free parameters. Thus, the number of free parameters required to model the entire experimental spectrum in Fig. 12 is reduced to eight. The curve resulting from the fit is also depicted in Fig. 12 as the solid line through the data points. The photon bandwidth W thus determined was 48 meV. Other spectroscopic values extracted from the fit are summarized in Table V and compared with those from other measurements by Püttner $et\ al.$[8] and Coreno $et\ al.$[81] The three measurements are in good agreement, confirming that the parameters describing the potential of the core-excited state are well-established.

3.2   Resonant Auger spectra after O 1s → 2π excitation

The upper panels of Figs. 13(a)–13(c) show electron emission spectra recorded at three photon energies across the O 1s → 2π resonance; i.e., at 533.90, 534.20, and 534.62 eV, corresponding to the $v' = 3$, 5, and 8 excitations, respectively, in the core-excited state.[50] The bandwidths of the photon monochromator and electron analyzer were 59 and 31 meV, respectively, while the Doppler broadening was estimated to be 54 meV. Each spectrum shows the two bands corresponding to the transitions to the X 5σ⁻¹ ²Σ⁺ and A 1π⁻¹ ²Π electronic final states in the binding energy range 13.4–19.4 eV. Here, binding energy for each detected electron is given by photon energy − electron kinetic
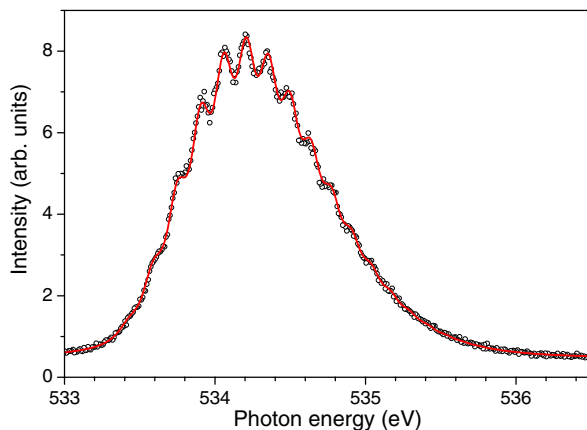

Fig. 12.   (Color online) O 1s → 2π total ion yield spectrum of CO. The solid line represents the best fit of the experimental data points (filled circles). The monochromator function for this curve was taken to be of Gaussian shape having a FWHM of 48 meV. From ref. 50.

spectrum,[80] taking as adjustable parameters the Gaussian width W (representing the photon bandwidth), the Lorentzian width Γ (representing the lifetime width), the level of a constant background, and the energy and height of the first peak in the progression. The positions and heights of all other peaks in the progression are determined by the potential energy curves and nuclear wave functions of the ground and core-excited states. The accurately known
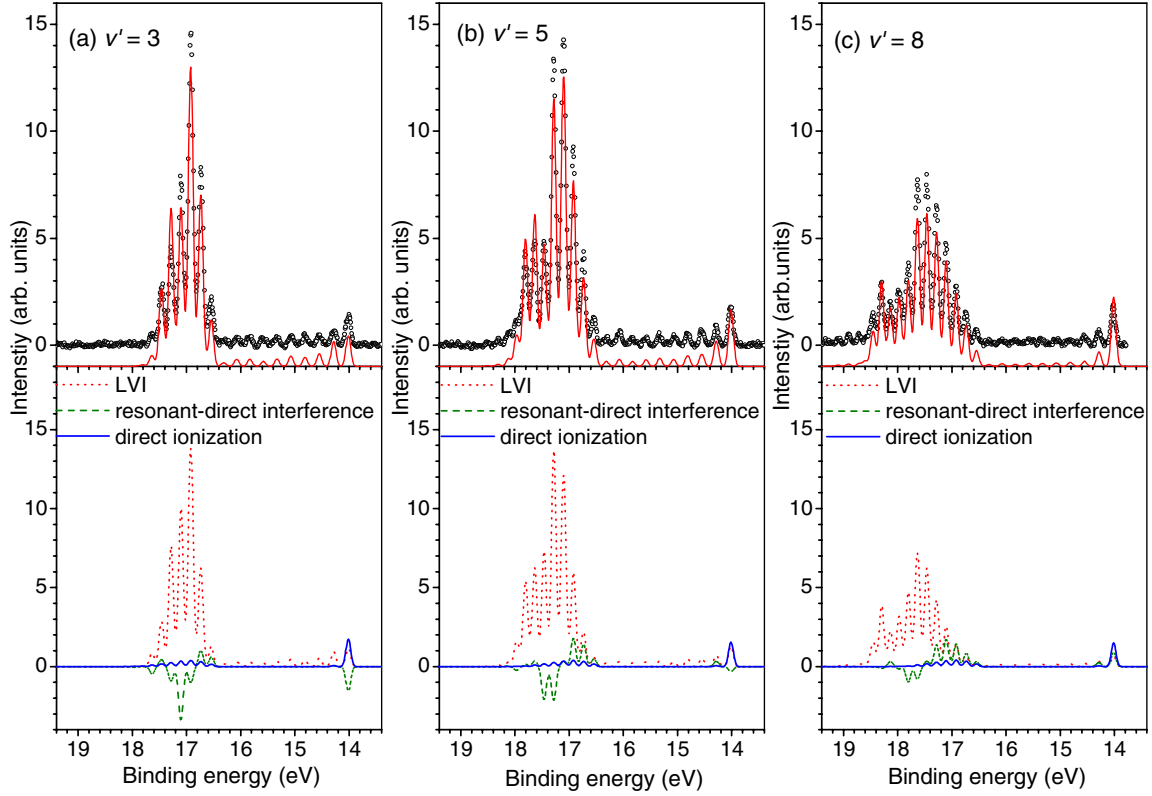
Fig. 13. (Color online) Upper panel: Comparison between measured and simulated spectra via excitation to (a) $v' = 3$, (b) 5, and (c) 8 of O $1s^{-1}2\pi$ core-excited state. See text for the details. Lower panel: direct, resonant (LVI), and direct-resonant interference terms defined by eq. (15). From ref. 50.

energy. The vibrational distribution in the A state varies significantly as the vibrational quantum number v' of the intermediate core-excited state increases from 3 to 8. With the increase in v', higher vibrational components appear and form the second peak in the vibrational distribution at $v'' = 6$ for $v' = 5$ and at $v'' = 10$ for $v' = 8$, where v'' is the vibrational quantum number excited in the ionic A $1\pi^{-1}\ ^2\Pi$ state. The X band, on the other hand, also shows resonant enhancement but their v'-dependence of the v''-distribution is less significant than that of the A band.

The resonant photoemission spectrum can be described as[10,80]

$$I_f(\omega) = \left| D\langle f|0\rangle + M \sum_n \frac{\langle f|n\rangle\langle n|0\rangle}{\omega - \omega_{n0} + i\frac{\Gamma}{2}} \right|^2, \quad (14)$$

where the first and second terms stand for the direct and resonant photoionizations, respectively, D and M are the electronic transition moments of the relevant channels, $|0\rangle$, $|n\rangle$, $|f\rangle$ denote vibrational wave functions of the initial ground state, intermediate core-excited state, and final ionic state, respectively, Γ is the lifetime width of the core-excited state, and ω_{n0} is the energy of the core-excited vibrational state $|n\rangle$ relative to the ground vibrational state $|0\rangle$). We have simulated the resonant Auger spectra using eq. (14) for each of the two bands X and A. The vibrational wave functions $|0\rangle$ and $|f\rangle$ for the initial ground state and the final ionic state of the resonant Auger process are calculated using the spectroscopic constants of these states given in ref. 82, whereas the vibrational wave functions $|n\rangle$ for the intermediate core-excited state are calculated using the constants

in Table V. The ratio of $|D/M|^2$ for each band was determined so that the intensity ratios of the direct and resonant spectra were equal in the experimental and simulated spectra. Positive values were chosen for both M and D for both bands since choosing one of them to have a negative value worsened the agreement with the experiment significantly. In the upper panels of Figs. 13(a)–13(c), the spectra simulated using eq. (14) are compared with the experimental spectra.

To investigate the interference between the resonant and direct photoemission channels explicitly, we rewrite eq. (14) as

$$I_f(\omega) = I_f^{\text{LVI}}(\omega) + |D\langle f|0\rangle|^2 + \sum_n \frac{2DM(\omega - \omega_{n0})}{(\omega - \omega_{n0})^2 + \frac{\Gamma^2}{4}}, \quad (15)$$

where

$$I_f^{\text{LVI}}(\omega) = |M|^2 \left| \sum_n \frac{\langle f|n\rangle\langle n|0\rangle}{\omega - \omega_{n0} + i\frac{\Gamma}{2}} \right|^2 \quad (16)$$

represents the LVI-modified resonant emission. The second term represents the direct portion of the emission intensity and the third term represents the interference between the resonant and direct photoemission channels. In the lower panels of Figs. 13(a)–13(c), we plot these three contributions separately. Let us focus on the A band. Although the direct photoemission intensity $|D\langle f|0\rangle|^2$ is indeed negligible in comparison with the resonant contribution $I_f^{\text{LVI}}(\omega)$, the resonant–direct interference term [the third term of eq. (15)] significantly contributes to the total intensity $I_f(\omega)$. If

one compares the contribution from each of these channels to the A band intensity, examining the lower panels of Fig. 13, one notices that the contribution from the LVI term and that from the resonant–direct interference term in eq. (15) cancel out. This explains how the agreement between the simulated and measured spectra is improved by taking the interference between the resonant and direct emission channels into account.

4. O 1s excitation/de-excitation of H_2O

4.1 O 1s total and partial ion yield spectra

The H_2O molecule has a geometric structure that belongs to the C_{2v} point group (R(O–H) = 0.958 Å; θ_{H-O-H} = 104.4°)[83]) in the ground state, and the electronic configuration is[84]

$$1a_1^2\ 2a_1^2\ 1b_2^2\ 3a_1^2\ 1b_1^2;\ 4a_1^0\ 2b_2^0\ X\ ^1A_1.$$

Here, $1a_1$ and $2a_1$ are O 1s and O 2s orbitals, respectively. The outermost orbital $1b_1$ has mostly the out-of-plane O $2p_x$ character, while the in-plane components O $2p_z$ and O $2p_y$ combine with H 1s and form the O–H bonding orbitals $3a_1$ and $1b_2$, respectively. The unoccupied orbitals $4a_1$ and $2b_2$ are the antibonding counterparts of these two orbitals. There are three vibrational modes in the H_2O molecule of C_{2v} point group; the symmetric stretching mode of a_1 symmetry, the bending mode of a_1 symmetry and the asymmetric stretching mode of b_2 symmetry.

Figure 14 shows the total ion yield spectrum of H_2O in the whole O 1s excitation region.[12]) The monochromator bandwidth is ~55 meV. The structures between 537 and 540 eV are due to the transitions to the Rydberg members.[5]) Okada et al.[11]) investigated vibrational structures of the Rydberg members in H_2O and D_2O, employing angle-resolved ion yield spectroscopy.[85]) The line at ~537.10 eV was assigned to a promotion of the O 1s electron to the degenerated Rydberg orbitals $3pa_1$ and $3pb_1$ and a shoulder structure at the high-energy side, at 537.25 eV in H_2O and at 537.21 eV in D_2O, was assigned to the excitation of the bending vibration in the O $1s^{-1}$ $3pa_1/3pb_1$ core-excited states. The vibrational spacing of 150 meV for H_2O is very close to that of 159 ± 5 meV for the O 1s ionized state of H_2O observed in the O 1s photoelectron spectrum.[86]) This

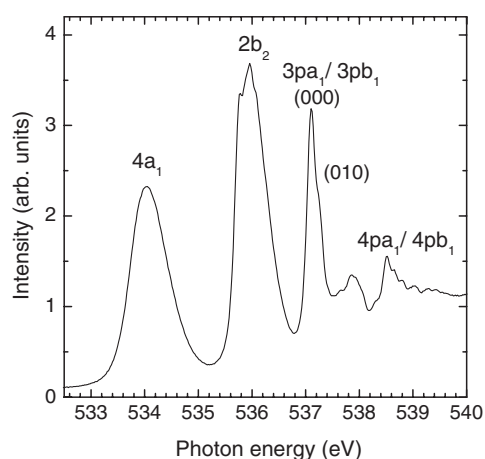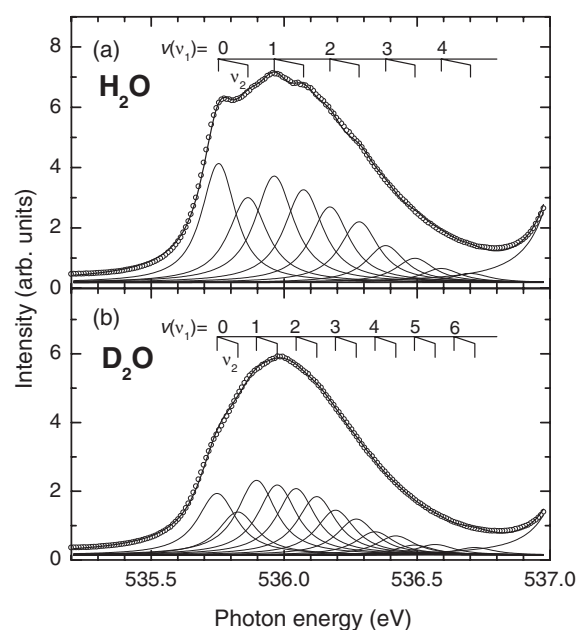Fig. 14. Total ion yield spectrum of H_2O in O 1s excitation region. From ref. 12.

Fig. 15. High-resolution (~40 meV) spectra of H_2O (a) and D_2O (b) in region of $2b_2$ band. The solid curves are the result of the least-squares peak fit. From ref. 12.

agreement is in accordance with the relatively pure non-bonding Rydberg character of the $3pa_1$ and $3pb_1$ orbitals.[11])

The broad bands at 534 eV ($4a_1$) and 536 eV ($2b_2$) correspond to the promotions of the electron from O 1s to the unoccupied antibonding molecular orbitals $4a_1$ and $2b_2$, respectively. The O 1s → $4a_1$ band shows no vibrational structure. This observation confirms the dissociative character of this state, as reported previously.[5]) In contrast to $4a_1$, the $2b_2$ band exhibits vibrational structures with obvious peaks at 535.74, 535.95, and 536.08 eV and a bump at 535.85 eV, as presented in the slightly higher resolution spectrum (bandwidth ~40 meV) in Fig. 15(a). The vibrational structures become less clear in the higher-energy side of the $2b_2$ band. The observed vibrational structure cannot be explained by a simple progression of one vibrational mode.

To proceed with the analysis of the vibrational structure, a least-squares peak fitting is carried out for the entire $2b_2$ band. In the peak fitting, two vibrational modes ν_1 and ν_2 both with constant vibrational spacing (harmonic approximation) are assumed and each peak is assumed as a convolution of a Gaussian profile with a 40 meV FWHM and a Lorentzian profile whose FWHM has a lower-limit value of 150 meV, i.e., the core-hole lifetime width,[87]) at the first peak at 535.74 eV, and increases linearly with the vibrational energy. The energy-dependent Lorentzian width was necessary for the reasonable fitting, suggesting that higher vibrational states are dissociative. The Lorentzian width as a function of vibrational energy E_{vib} turned out to be $0.15 + 0.1E_{vib}$ (eV) via the fitting. The vibrational spacings obtained via fitting are 215 ± 5 meV and 114 ± 5 meV, as seen in Fig. 15(a). An even number of ν_2 vibrational states may not be distinguished from the ν_1 sequence because the frequency of ν_1 is about twice that of ν_2. A similar analysis is carried out for D_2O as shown in Fig. 15(b). A reasonable fitting is obtained in the case of 151 ± 5 and 80 ± 5 meV for

ν_1 and ν_2, respectively, using a frequency reduction factor of 0.7 from H_2O to D_2O. The consistent fitting between H_2O and D_2O for the vibrational structures indicates the validity of the analysis and eliminates the possibility of the overlap of another electronic state in this resonance. The two vibrational modes ν_1 and ν_2 with vibrational frequencies 215 ± 5 and 114 ± 5 meV, respectively, can be assigned to symmetric stretching and bending vibrations (ν_1', ν_2') in the O $1s^{-1}2b_2$ core-excited state in H_2O. These two vibrational modes are strongly coupled.[12] It is worth noting that the values of the vibrational frequencies are significantly different from the values 460 ± 20 and 159 ± 5 meV for symmetric stretching and bending vibrations, respectively, for the O 1s ionized state.[86] This significant difference is in accordance with the valence antibonding character of the $2b_2$ orbital where the electron in promoted in the core-excited state.

Piancastelli *et al.* observed the H_2^+ formation from H_2O^+ via the O 1s $\rightarrow 2b_2$ excitation in H_2O.[88] They suggested a key role of the bending motion in the core-excited state, though they could not resolve the vibrations with their limited resolution (~ 180 meV bandwidth) and thus could not exclude the possibility of the overlap with another electronic state. In a similar measurement with a bandwidth of ~ 55 meV,[12] vibrations in the core-excited state are resolved and clear evidence is obtained for the role of the vibrations in the core-excited state.

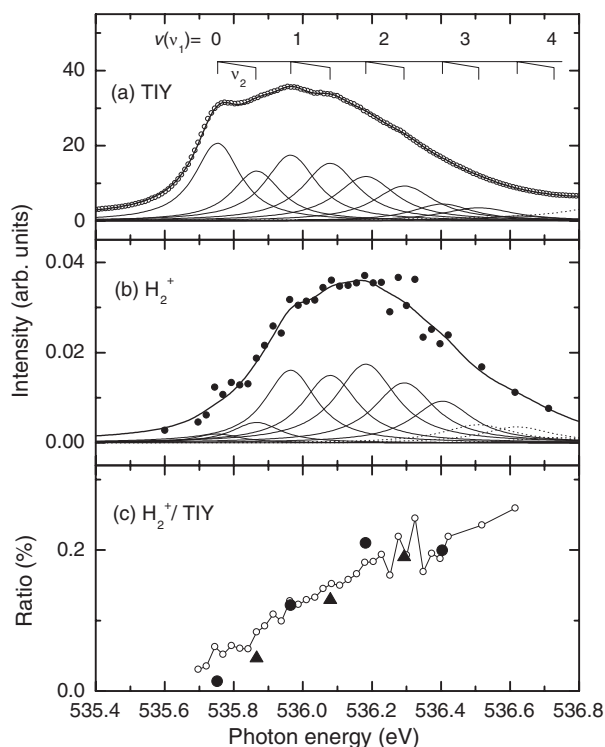Figure 16 shows the H_2^+ ion yield curve (b) and the intensity ratio of H_2^+ (c) relative to the total ion given in (a), as a function of the excitation photon energy. The H_2^+ ion yield curve is analyzed in the same way as the total ion curve, and the intensity ratio H_2^+ to the total ion for each vibrational quantum state is also plotted in Fig. 16(c). The reaction rate for the H_2^+ formation increases linearly with the internal energy stored in the O $1s^{-1}2b_2$ core-excited state. The linear dependence of the H_2^+ formation on the internal energy of the core-excited state clearly demonstrates that the H_2^+ formation is mediated by the nuclear motion in the core-excited state. The fact that H_2^+ formation is independent of excited vibrational modes, ν_1 or ν_2, is in accordance with the theoretical prediction that the symmetric stretching and bending motions are coupled.

4.2 Resonant Auger spectra after O 1s excitation

Previously, Hjelte *et al.* recorded the resonant Auger spectra of H_2O at the O 1s $\rightarrow 4a_1$ excitation at MaxII and found the electron emission from the OH fragment as clear evidence of a molecular dissociation that is faster than the Auger decay, often called *ultrafast dissociation*.[37] Here, we focus on the O 1s $\rightarrow 2b_2$ excitation (see Figs. 15 and 16). It is shown that the two-dimensional nuclear motion of the Auger final state can be probed by resonant Auger spectroscopy and furthermore that it can be mediated by sampling a different portion of the potential curve and changing the nuclear motion in the core-excited state.[39,48]

Figure 17 presents the electron spectra of H_2O in the binding energy interval of the valence-ionized states $X(1b_1^{-1})$, $A(3a_1^{-1})$ and $B(1b_2^{-1})$. The vibrational components in the core-excited state are labeled (ν_1', ν_2'), with ν_1' and ν_2' being the quantum numbers for symmetric stretching and

Fig. 16. Total ion yield spectrum (a), H_2^+ yield spectrum (b) and ratio of H_2^+ to total ion (c) in O $1s^{-1}2b_2$ resonance. Solid line in (b), fitting to experimental results given by full dots. The scatter of the dots indicates the experimental uncertainties. Open circles in (c), estimated from yield curves in (a) and (b). Closed circles and triangles in (c), estimated from area of each vibrational component in (a) and (b) obtained via least-squares fitting, for (ν_1', 0) and (ν_1', 1), respectively. From ref. 12.
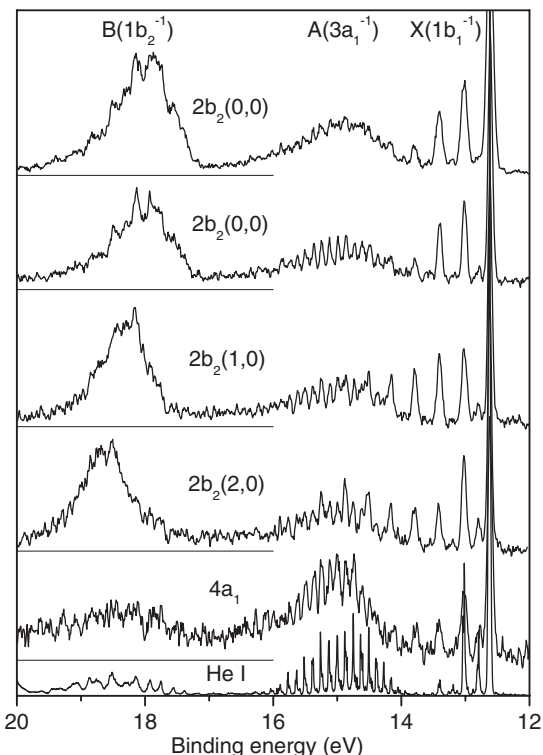

Fig. 17. Comparison between resonant Auger electron spectra of H_2O with direct photoemission (at the bottom). The top spectrum was recorded with the gas cell whereas all others under Doppler-free conditions. From ref. 48.

bending modes. The uppermost spectrum is recorded using the gas cell, whereas all others are recorded under Doppler-free conditions.[48] The spectrum at the bottom was recorded with a He I lamp, with a photon energy of 21.218 eV, and is presented here only for comparison. The other spectra were recorded at photon energies corresponding to O 1s → 2b$_2$ excitation with (0, 0), (1, 0) and (2, 0). The photon width and the width of the electron analyzer were about 40 and 33 meV, respectively.

First, let us compare the spectra recorded at the O 1s → 2b$_2$ (0, 0) excitation with the gas cell and under Doppler-free conditions. The X band is dominated by the $(v_1'', 0)$ progression corresponding to the symmetric stretching with a spacing of 398 meV[89] and starting at 12.62 eV. In the Doppler-free spectrum, it is clear that the vibrational progression $(v_1'', 1)$, starting at the energy of 12.78 eV is also excited. In the gas-cell spectrum, the resolution is not sufficiently high for us to say whether the A band contains more than one vibrational progression, whereas in the Doppler-free spectrum, it is clear that only the bending progression $(0, v_2'')$ with a frequency of 108 meV[89] is present; the stretching mode has a frequency of 439 meV and is not present.

Let us now focus on the X band. The progression of the symmetric stretching vibrations with a vibrational spacing of ∼400 meV is clearly observed. The enhancement of the higher vibrational components $(v_1'', 0)$ with $v_1'' \geq 4$ in the X band becomes significant when higher vibrational components $(v_1', 0)$ with $v_1' \geq 1$ are excited in the O $1s^{-1}2b_2$ state. Note that, if the lifetime of the core-excited state were zero, the vibrational distribution would be the same for all the spectra. The symmetric stretching vibration is, however, more excited in the X state when it is populated by the resonant Auger process via the higher vibrational component of the core-excited state. The reason for this is that the symmetric stretching motion proceeds in the core-excited state before vibrational energy is transferred to the Auger final state.

Let us now focus on the B band and compare the resonant spectra with the direct photoemission spectra (the bottom spectrum). In either the gas-cell or Doppler-free spectrum, we cannot entirely resolve the vibrations and thus cannot surely say to what extent the stretching and bending progressions are excited. The spacings of the stretching and bending modes in this band are 368 and 198 meV, respectively.[89] Thus, if only one of the two modes was excited, we could see the progression. It seems the reason why the vibrational structure is not clearly resolved is because of multimode vibrational excitations in the final states. Note also that this B state may be predissociative for the vibrational components above 18 eV.[49]

Let us now discuss the photon energy dependence. The centroid of the B band shifts towards a higher binding energy, indicating that higher vibrational components are excited in the $1b_2^{-1}$ Auger final state. With the help of *ab initio* calculation, De Fanis *et al.* concluded that the reason why the vibrational structure in the B band is less resolved at higher energies is because the multimode vibrational excitation becomes increasingly more complex in the $1b_2^{-1}$ Auger final state with the increase in the vibrational excitation in the core-excited state.[39] Even with the

unprecedented resolution achieved by Doppler-free spectroscopy, however, it is still not possible to extract the intensity of each vibrational component.

At the O 1s → 4a$_1$ excitation, only the A band is enhanced. The vibrational progression remains similar to the one in the direct photoemission, dominated by the bending mode, without the presence of the stretching mode. This result is in contrast with that of Hjelte *et al.*, where the limited resolution made the authors conclude that more than one vibrational progression was present.[37]

4.3 Resonant Auger spectra after above-threshold excitation

In the above-threshold region, the photoabsorption curve is rather flat, without pronounced resonant features.[12] However, in one particular experiment, namely, negative ion yield spectroscopy, it has been possible to identify a resonant feature ∼10 eV above the ionization threshold.[90] This feature has to be related to doubly excited states, since it is well known that there are no shape resonances in H$_2$O.[91]

In Fig. 18(a), we show the total ion yield spectrum and the angle-resolved ion yield spectra recorded in the directions 0° and 90° with respect to the polarization vector. These spectra were recorded at SPring-8. All spectra look rather flat in the photon energy region above the ionization threshold (539.6 eV). Figure 18(b) displays partial ion yield spectra of negative fragments O$^-$ and H$^-$. These spectra were recorded by Stolte *et al.* at the Advanced Light Source in U.S.A. (see ref. 90). A broad resonance appears at ∼10 eV above the threshold only in the O$^-$ negative ion yields.
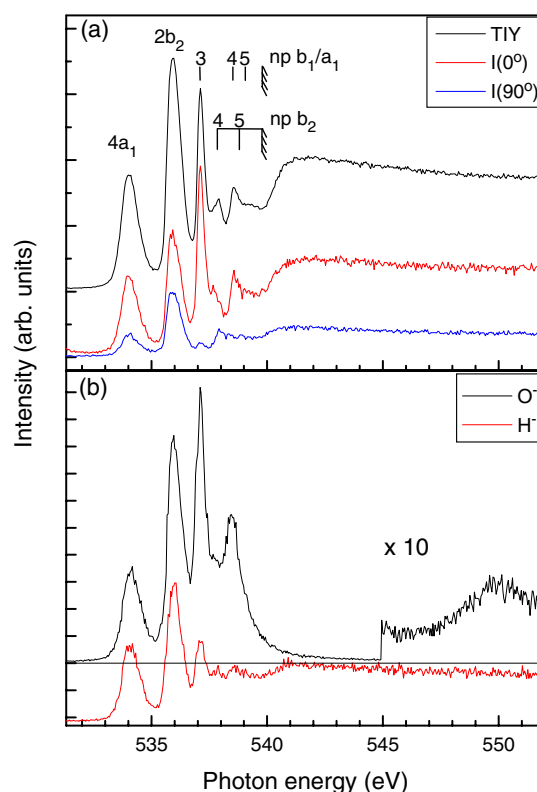

Fig. 18.   (Color online) Total and angle-resolved ion yield spectra (a), and H$^-$ and O$^-$ yield spectra (b) in O 1s excitation region. From ref. 47.
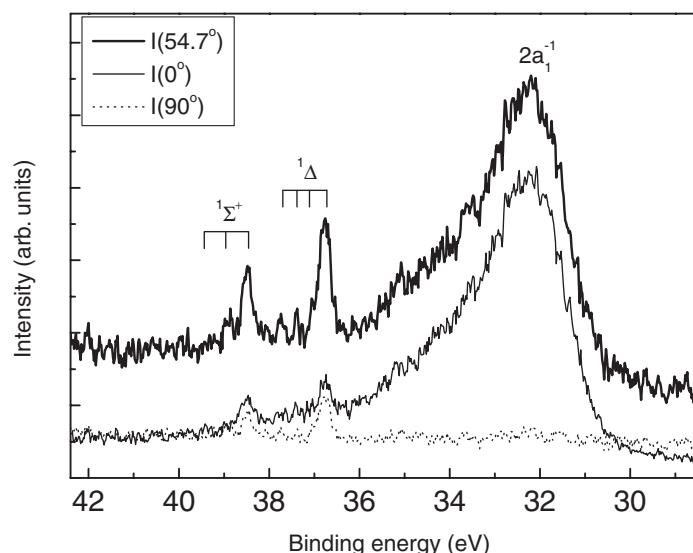
Fig. 19. Resonant Auger spectrum recorded on top of resonance at 550 eV photon energy; see Fig. 18(b). From ref. 47.

Piancastelli *et al.* recorded electron spectra at several photon energies across the broad resonance that appeared only in the O^- yields above the threshold.[47] The aim was at trying to characterize the possible increase in relative intensity of spectral features related to single-hole final states, and/or verifying the presence of lines arising from the resonant Auger decay of the OH fragment produced by dissociation faster than the Auger decay, rather than from the decay of the intact molecule. As noted in the previous subsection, ultrafast dissociation was investigated in H_2O resonantly excited below the O K-edge and the decay spectrum of the OH fragment was well characterized in a previous work by Hjelte *et al.*[37]

In Fig. 19, we show electron spectra, $I(0°)$ and $I(90°)$, recorded in the directions $0°$ and $90°$, respectively, with respect to the polarization vector, and the angle-integrated spectrum as given by $I(0°) + 2I(90°)$. The employed photon energy 550 eV corresponds to the maximum of the resonance identified in the negative ion yield curves. The spectra exhibit a broad feature at a binding energy of 32 eV, which corresponds to the electron binding energy of inner-valence molecular orbital $2a_1$. Superimposed to it, some sharp structures with vibrational substructure appear in the binding energy range between 36 and 40 eV. The relative position of the features and their vibrational spacing are consistent with the Auger spectrum of the OH fragment.[37]

As a further test, the spectrum was measured at several different photon energies across the broad resonance. The broad molecular feature at a binding energy of 32 eV changes its electron kinetic energy linearly as a function of photon energy, thus remaining at a constant binding energy. The electron kinetic energies corresponding to the sharp structures, on the other hand, stay constant, even though the photon energy is changed. Such behavior is typical of spectral features related to fragments.[37] We can assign these sharp peaks to the electronic decay of the OH radical, as indicated in Fig. 19. Thus, we can conclude that the resonant state at ~ 10 eV above the threshold, evident only in the O^- yields, is dissociative, as proven by the appearance of fragment-related spectral structures.

It is worth noting that the reaction channel that leads to electron emission from the OH^* core-excited fragment described here is different from the one that leads to the O^- yield. The former reaction channel produces an OH^+ anion via the reaction $OH^* \rightarrow OH^+ + e^-$(Auger), while the latter may be speculated as due to radiative decay from the OH^* fragment to the ion-pair state; $OH^* \rightarrow OH + h\nu \rightarrow O^- + H^+$. To draw a decisive conclusion for the reaction channel of the O^- yield from this resonant state, however, further investigations are indispensable.

5. F 1s Excitation/De-excitation in CF_4

The ground-state electronic configuration of a CF_4 molecule, which belongs to a T_d point group in its ground state, is

$$(\text{core}) \; 1a_1^2 \; 1t_2^6 \; 2a_1^2 \; 2t_2^6 \; 1e^4 \; 3t_2^6 \; 1t_1^6; \; 3a_1^{*0} \; 4t_2^{*0} \; X \; {}^1A_1.$$

Here, "(core)" includes F 1s and C 1s. $2a_1$ and $2t_2$ have C–F bonding character. The unoccupied orbitals $3a_1^*$ and $4t_2^*$ are counterparts of these two and have antibonding character.

5.1 Angle-resolved ion yield spectra in F 1s excitation region

In Fig. 20, we present ion yield spectra of the CF_4 molecule near the F 1s ionization threshold.[41] The top panel shows the total ion yield spectrum recorded using the ion detector for 4π sr collection, whereas the middle panel shows the angle-resolved yield spectra, $I(0°)$ and $I(90°)$, of energetic fragment ions with a kinetic energy larger than 6 eV, recorded using the two identical retarding-potential ion detectors placed in the directions parallel and perpendicular to the polarization vector of the light. Values of the photoion anisotropy parameter β obtained from $I(0°)$ and $I(90°)$ are also plotted in Fig. 20 (bottom panel). The largest anisotropy of $\beta \sim 0.36$ is around the weak shoulder structure A at ~ 690 eV.

We discuss the origin of the preferential dissociation along the polarization vector of the light. To do so, we start with the symmetry-adapted molecular orbital picture.[92,93] Then, the F 1s shell forms symmetry-adapted t_2 and a_1
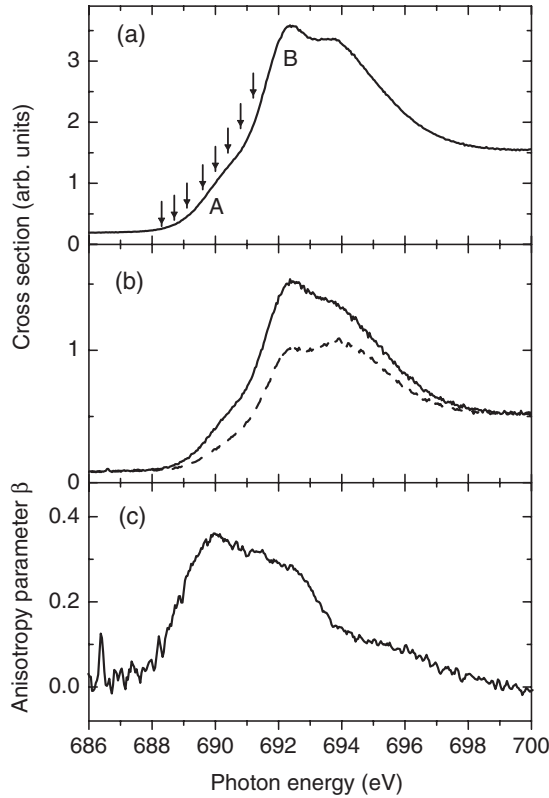
Fig. 20. (a) Total ion yield spectrum in F 1s excitation region of CF_4 molecule. (b) Yield spectra of energetic ions measured in directions parallel and perpendicular to polarization vector of light (solid and dashed lines, respectively). (c) Photoion anisotropy parameter β extracted from angle-resolved spectra. The photon energies used in the Auger decay study are indicated by arrows on the total ion yield spectrum. From ref. 41.

We can take the axis of the F^+ ion ejection to be the $F^{(1)}$–C axis (i.e., z-axis) without loss of generalization. The ion detectors are mounted parallel (0°) and perpendicular (90°) to the polarization vector of the light. F^+ detection at 0° corresponds to events in which the $F^{(1)}$–C axis (z-axis) coincides with the polarization vector of the light and thus the $T_2^*(z)$ component given by eq. (20) is excited. In this case, referring to eq. (20), we find that there is a significant possibility that $F^{(1)}$ has a F 1s hole. On the other hand, the F^+ detection at 90° corresponds to the events in which the $F^{(1)}$–C axis (z-axis) is perpendicular to the polarization vector, within the x–y plane, and thus $T_2^*(x)$ and $T_2^*(y)$ components given by eqs. (18) and (19) are excited. Then, referring to eqs. (18) and (19), we find that there is no possibility that $F^{(1)}$ has a F 1s hole. Thus, the positive value of $\beta \simeq 0.36$ at the feature A in Fig. 20 is attributed to the preferential rupture of the F–C bond along the axis where the F core-hole is situated. It should be noted that even if asymmetric nuclear motion does not occur in the core-excited state, Auger decay can transfer the alignment to the Auger final state, where asymmetric nuclear motion in the Auger final state may result in anisotropic ionic fragmentation. The ion yield measurement cannot distinguish symmetry breaking in the core-excited state from that in the Auger final state.

5.2 Auger emission from F fragments

Figure 21 shows a series of electron-emission spectra from the decay of core-excited states in CF_4 with energies close to 690 eV. The measurements were made at 8 different

molecular orbitals in CF_4. Dipole-allowed transitions from F 1s a_1 lead to t_2^*, whereas those from F 1s t_2 lead to both a_1^* and t_2^*. In analogy with the case of SiF_4,[94] the main peak B in Fig. 20 may correspond primarily to the F 1s a_1, $t_2 \rightarrow t_2^*$ excitation, whereas the weak feature A is assigned to the F 1s $t_2 \rightarrow a_1^*$ excitation. Introducing the molecular frame axis z that coincides with one of the four F–C axes and the x-axis in such a way that one of the other three F atoms lies in the x–z plane, we can label the F atom on the z-axis $F^{(1)}$, that on the x–z plane $F^{(2)}$ and the other two $F^{(3)}$ and $F^{(4)}$. Using the localized-hole wave functions $\Phi_i \equiv F^{(i)}$ $1s^{-1}$ a_1^* as a basis set, we can express symmetry-adapted wave functions of the core-excited states F 1s $a_1^{-1} a_1^*$ A_1^* and F 1s $t_2^{-1} a_1^*$ T_2^* in the following manner:

$$A_1^* = \frac{1}{2}(\Phi_1 + \Phi_2 + \Phi_3 + \Phi_4), \qquad (17)$$

$$T_2^*(x) = \frac{1}{\sqrt{6}}(2\Phi_2 - \Phi_3 - \Phi_4), \qquad (18)$$

$$T_2^*(y) = \frac{1}{\sqrt{2}}(\Phi_3 - \Phi_4), \qquad (19)$$

$$T_2^*(z) = \frac{1}{\sqrt{12}}(3\Phi_1 - \Phi_2 - \Phi_3 - \Phi_4). \qquad (20)$$

Photoabsorption from the A_1 ground state to A_1^* is dipole forbidden. The transitions to the three degenerate T_2^* states are allowed, where x, y, z labeled for the three components of T_2^* give the directions of the transition dipole moments.
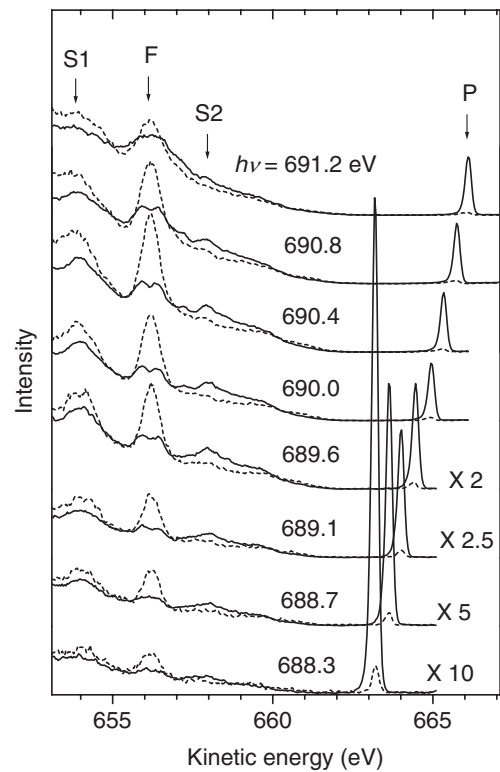

Fig. 21. Angle-resolved electron spectra recorded across F 1s $\rightarrow a_1^*$ resonance for 8 different photon energies indicated by arrows in Fig. 20. The dotted line is the measurement with the electron spectrometer lens mounted perpendicular to the polarization vector of the light, and the solid line is the in-plane measurement. From ref. 41.
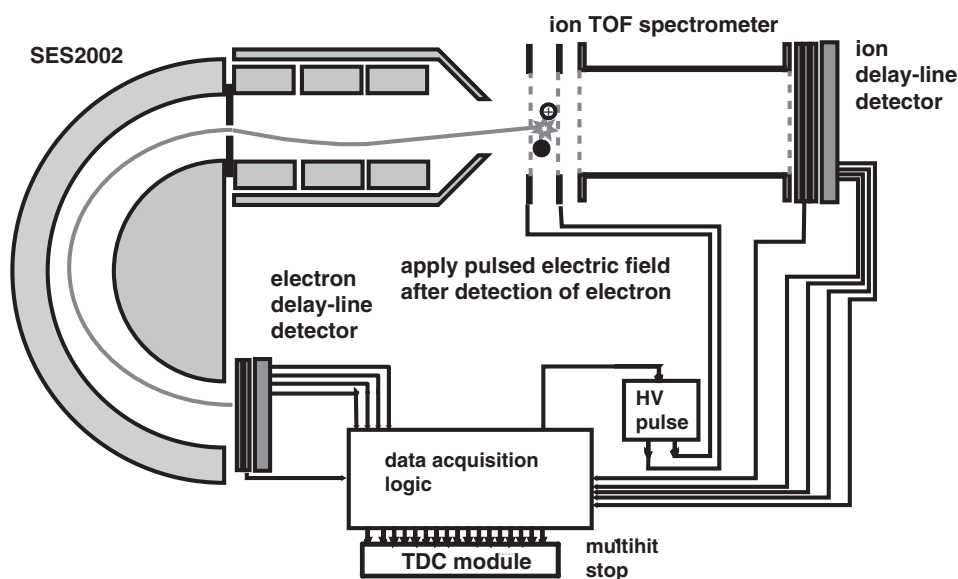
Fig. 22. Schematic diagram of experimental setup for Auger-electron ion coincidence momentum imaging. See the text for details.

photon energies indicated by arrows in Fig. 20, at angles both parallel and perpendicular to the polarization vector of the light.[41] The spectral feature P disperses linearly in kinetic energy as the photon energy is tuned through the state; this feature corresponds to the D $^2A_1$ photoelectron band. The spectral feature F at $\sim$656.2 eV, on the other hand, remains at the same kinetic energy in all spectra. The broader features S1 and S2 also appear at fixed kinetic energies of $\sim$654 and $\sim$658 eV. This nondispersive behavior stems from transitions between potential energy surfaces that are locally parallel. At the limit of large distances, the transition is between levels in a fragment. The excess kinetic energy is transferred to the kinetic energy of the fragment. Looking more closely at peak F, we find that the spectra measured around 690 eV show a double-peak structure at 0°. This behavior is indicative of the Doppler-like splitting measured previously in, for example, O_2.[35] If the dissociation of the molecule occurs on a time scale comparable to the Auger decay, and takes place preferentially along the polarization vector of the light, then electron emission can be observed with Doppler shifts due to the motion of the fragment that emits the electron. The Doppler shift of the electron kinetic energy for the fragments propagating in opposite directions has the opposite sign. The double peak structure in the 0° spectrum corresponds to this Doppler splitting. When dissociation takes place preferentially along the axis perpendicular to the observer, the direction of the dissociation is symmetric with respect to the measurement direction. Thus, the Auger electron emitted from the departing fragment results in a single-peak structure as seen in the 90° spectrum. The observation of the Auger emission of the atomiclike F* fragment and its Doppler splitting in the 0° spectrum is direct evidence that the asymmetric nuclear motion proceeds in the F 1s core-excited state.

We now consider how this asymmetric nuclear motion is caused. The F $1s^{-1}a_1^*$ core-excited states consist of nearly degenerate A_1^* and T_2^* states. A coupling between the electron motion and the asymmetric nuclear motion causes pseudo-Jahn–Teller mixing between these A_1^* and T_2^* core-

excited states, in addition to the Jahn–Teller mixing within T_2^*. When one C–F bond is elongated, the molecule belongs to the C_{3v} point group. The T_2^* state splits into the A_1^* and E^* components. The A_1^* couples with the other A_1^* that originates from the A_1^* in T_d geometry. As a result of these couplings, one of the A_1^* potential energy curves is expected to be strongly repulsive along the asymmetric stretching coordinate. This mechanism leads to fast fragmentation along one C–F axis and results in Auger electron emission from the departing fragment.

One may also address the question of whether the observed atomiclike electron emission necessarily takes place at the dissociation limit. The dissociation is not complete within the F 1s hole lifetime in a strict sense. We will discuss this specific aspect below.

5.3 Intramolecular scattering of Auger electron

More detailed insight into the process can be gained by measuring the emitted Auger electron in coincidence with the emitting fragment.[95,96] This type of coincidence experiment in fact provides evidence that a significant fraction of the Auger electrons emitted from the atomic F fragment undergoes intramolecular scattering on the other fragment CF_3.[51]

The experimental setup and data acquisition system are shown schematically in Fig. 22 and are described in detail in refs. 96 and 97. Briefly, the setup consists of a hemispherical electron spectrometer (Gammadata-Scienta SES-2002) and an ion time-of-flight (TOF) spectrometer mounted inside a vacuum chamber. In order to make coincidence experiments possible, a standard CCD camera of the electron spectrometer was replaced by a delay-line detector (Roentdek DLD40).[98] During the coincidence experiment, all voltages of the electron spectrometer were fixed. The sample gas (CF_4 in the present case) is introduced at the center of the pusher and extractor electrodes of the ion spectrometer through a *grounded* copper needle. Electrons pass the *grounded* pusher electrode and enter the electron spectrometer. Triggered by the electron detection, rectangular high-
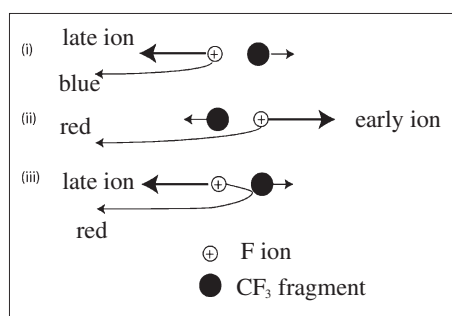
Fig. 23. Schematic diagram of processes detected in present coincidence experiment. Only the electrons ejected in the left direction are detected. Processes (i) and (ii) without scattering can be detected as coincidence events between blueshifted electrons and late ions, and between red-shifted electrons and early ions, respectively, whereas process (iii) involving backscattering can be detected as coincidence events between redshifted electrons and late ions. From ref. 51.

voltage pulses with opposite signs are generated by a specially designed pulse generator (GPTA HVC-1000)[99] and applied to the pusher and extractor electrodes. The ions are extracted by this pulsed *uniform* electric field and detected by another delay-line detector with an active diameter of 80 mm (Roentdek DLD80)[98] set at the end of the TOF drift tube. All data is recorded in two 8-channel TDC (Roentdeck TDC-8)[98] modules. The data is stored in the list mode for off-line analysis.

We consider only events where an electron and an F^+ ion are detected in coincidence. Different contributions to the events detected in the coincidence experiment are illustrated in Fig. 23. To detect the electron, it must be emitted in the direction of the entrance slit of the electron spectrometer, whereas the F^* atom may fly in any direction. For simplicity, only the F^* atoms flying to the left and right are shown in the figure. These are the most common cases, because the fragmentation preferentially takes place along the linear polarization direction of the light.[41] Processes (i) and (ii)

involve only direct emission of the electron without scattering. Thus, the "red"- and "blue"-shifted electrons always correspond to a shorter or larger TOF of the ions, respectively, where the TOF is compared with the TOF of a nonenergetic F^+ ion. The ions are termed "early" and "late" accordingly.

Figure 24 shows an example of the data sets. Each point in the coincidence map (c) corresponds to one electron–ion coincidence event. Below the F^+ Auger peak in the electron spectrum (a), two clusters of points are visible in the map (c). They belong to processes (i) and (ii) in Fig. 23, i.e., coincidence events between blueshifted electrons and late ions and those between redshifted electrons and early ions, respectively. The diagonal line that crosses these two clusters of points shows the expected correlation between the ion TOF and the electron kinetic energy, which is calculated on the basis of knowledge of the fields in the ion spectrometer, which gives the relationship between the TOF and the ion momentum. Knowing the ion momentum, the Doppler shift of the electron can be calculated. The fact that the events scatter symmetrically around this line indicates that the electron is emitted when the ion has already reached its final speed. Thus, the Auger decay takes place in the atomic regime. An earlier emission must lead to a smaller Doppler shift of the electron. Thus, our observation is direct proof that the first phase of the fragmentation, the acceleration of the core-excited F^* atom, is faster than the Auger decay.

If a significant fraction of the electrons that are emitted in the direction of CF_3 undergo intramolecular scattering, the count rate for process (ii) will be reduced because the electron is no longer detected and, instead, process (iii) in Fig. 23 is detected for electrons that are initially emitted away from the electron detector and then reflected in its direction. Process (iii) can be distinguished from processes (i) and (ii) as a coincidence signal between the redshifted electron and the late ion. The degree of early–late asymmetry (the probability of backscattering) may be defined as
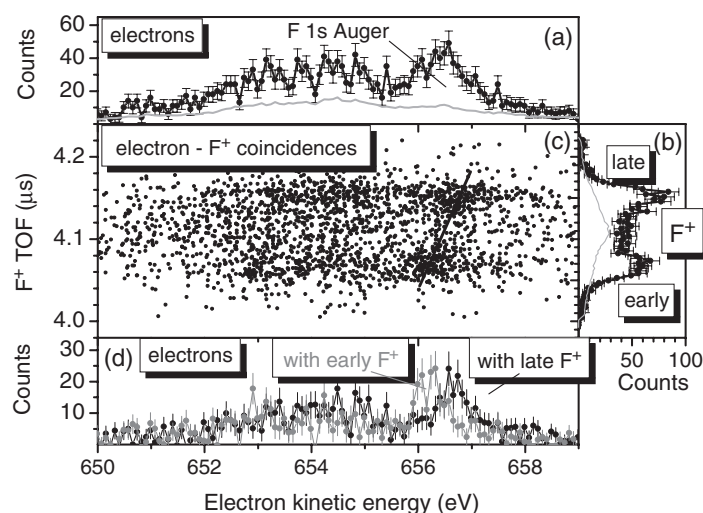

Fig. 24. (a) Electron spectrum coincident with F^+ ions. (b) F^+ ion TOF spectrum coincident with electrons in (a). The black data points in (a) and (b) are all coincident counts. The gray lines below are the random contributions. (c) Coincidence map. Each event is represented by a dot. (d) Electron spectra that are coincident with "early" and "late" F^+ ions, as illustrated in (b). In this graph, the contribution of the random coincidence has been subtracted. The photon energy was 689.4 eV. From ref. 51.
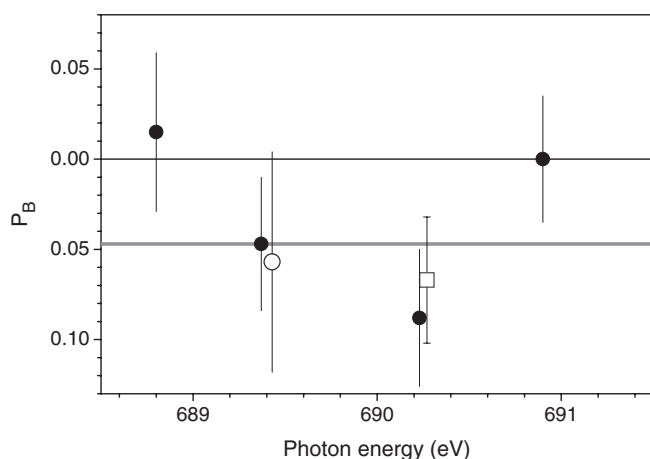
Fig. 25. Early/late asymmetry of ion TOF peak P_B as measure of strength of backscattering of Auger electron at CF_3 remainder. The different marks are from different beam times using the same apparatus. The gray line is the weighted average of all data points. From ref. 51.

$$P_B = \frac{I_e - I_l}{I_e + I_l}, \qquad (21)$$

where I_e and I_l are the integrated intensities (areas) of the early and late ions, respectively, as illustrated in Fig. 24(b). The results for the early–late asymmetry are shown in Fig. 25. The backscattering is found to be significant: it has an average value of $P_B = -4.7\%$ of the total coincident intensity.

6. Conclusion

The work discussed in this review demonstrates how recent technical advances, in light sources, high-resolution electron spectroscopy apparatus, and their experimental deployment, have made atomic and molecular core excitation and de-excitation spectroscopic studies in the soft X-ray regions an extremely powerful probe of atomic and molecular excitation and electronic de-excitation processes. The new experiments provide extremely rich data, with details not only on spectroscopic information about the core-excited states but also on dynamical interference effects in the excitation and de-excitation processes as well as about nuclear dynamics in the core-excited states and Auger final states. This powerful technique can be used to develop and test both quantum mechanical models and chemical insights of the photoexcitation and de-excitation processes.

1) K. Ueda: J. Phys. B **36** (2003) R1.
2) C. T. Chen, Y. Ma and F. Sette: Phys. Rev. A **40** (1989) 6737.
3) F. X. Gadea, H. Köppel, J. Schirmer, L. S. Cederbaum, K. J. Randall, A. M. Bradshaw, Y. Ma, F. Sette and C. T. Chen: Phys. Rev. Lett. **66** (1991) 883.
4) G. Remmers, M. Domke and G. Kaindl: Phys. Rev. A **47** (1993) 3085.
5) J. Schirmer, A. B. Trofimov, K. J. Randall, J. Feldhaus, A. M. Bradshaw, Y. Ma, C. T. Chen and F. Sette: Phys. Rev. A **47** (1993) 1136.
6) M. Coreno, L. Avaldi, R. Camilloni, K. C. Prince, M. de Simone, J. Karvonen, R. Colle and M. Simonucci: Phys. Rev. A **59** (1999) 2494.
7) M. Coreno, M. de Simone, K. C. Prince, R. Richiter, M. Vondrácek, L. Avaldi and R. Camilloni: Chem. Phys. Lett. **306** (1999) 269.
8) R. Püttner, I. Dominguez, T. J. Morgan, C. Cisneros, R. F. Fink, E. Rotenberg, T. Warwick, M. Domke, G. Kaindl and A. S. Schlachter: Phys. Rev. A **59** (1999) 3415.
9) K. C. Prince, L. Avaldi, M. Coreno, R. Camilloni and M. de Simone: J. Phys. B **32** (1999) 2551.
10) A. De Fanis, N. Saito, H. Yoshida, Y. Senba, Y. Tamenori, H. Ohashi, H. Tanaka and K. Ueda: Phys. Rev. Lett. **89** (2002) 243001.
11) K. Okada, K. Ueda, T. Tokushima, Y. Senba, H. Yoshida, Y. Shimizu, M. Simon, H. Chiba, H. Okumura, Y. Tamenori, H. Ohashi, N. Saito, S. Nagaoka, I. H. Suzuki, E. Ishiguro, I. Koyano, T. Ibuki and A. Hiraya: Chem. Phys. Lett. **326** (2000) 314.
12) A. Hiraya, K. Nobusada, M. Simon, K. Okada, T. Tokushima, Y. Senba, H. Yoshida, K. Kamimori, H. Okumura, Y. Shimizu, A.-L. Thomas, P. Millie, I. Koyano and K. Ueda: Phys. Rev. A **63** (2001) 042705.
13) H. Yoshida, K. Nobusada, K. Okada, S. Tanimoto, N. Saito, A. De Fanis and K. Ueda: Phys. Rev. Lett. **88** (2002) 083001.
14) K. Okada, H. Yoshida, Y. Senba, K. Kamimori, Y. Tamenori, H. Ohashi, K. Ueda and T. Ibuki: Phys. Rev. A **66** (2002) 032503.
15) A. Kivimäki, A. Naves de Brito, S. Aksela, H. Aksela, O.-P. Sairanen, A. Ausmees, S. J. Osborne, L. B. Dantas and S. Svensson: Phys. Rev. Lett. **71** (1993) 4307.
16) G. B. Armen, H. Aksela, T. Åberg and S. Aksela: J. Phys. B **33** (2000) R49.
17) A. Kivimäki, S. Heinäsmäki, M. Jurvansuu, S. Alitalo, E. Nommiste, H. Aksela and S. Aksela: J. Electron Spectrosc. Relat. Phenom. **114–116** (2001) 49.
18) Y. Shimizu, H. Yoshida, K. Okada, Y. Muramatsu, N. Saito, H. Ohashi, Y. Tamenori, S. Fritzsche, N. M. Kabachnik, H. Tanaka and K. Ueda: J. Phys. B **33** (2000) L685.
19) A. De Fanis, N. Saito, M. Kitajima, Y. Shimizu, K. Okada, H. Tanaka, I. Koyayo and K. Ueda: J. Phys. B **34** (2001) L377.
20) A. De Fanis, K. Ueda, N. Saito, M. Kitajima, H. Tanaka, Y. Shimizu, K. Okada and I. Koyayo: Surf. Rev. Lett. **9** (2002) 51.
21) K. Ueda, M. Kitajima, A. De Fanis, Y. Tamenori, H. Yamaoka, H. Shindo, T. Furuta, T. Tanaka, H. Tanaka, H. Yoshida, R. Sankari, S. Aksela, S. Fritzsche and N. M. Kabachnik: Phys. Rev. Lett. **90** (2003) 153005.
22) A. De Fanis, Y. Tamenori, M. Kitajima, H. Tanaka and K. Ueda: J. Electron Spectrosc. Relat. Phenom. **137–140** (2004) 271.
23) A. De Fanis, G. Prümper, U. Hergenhahn, M. Oura, M. Kitajima, T. Tanaka, H. Tanaka, S. Fritzsche, N. M. Kabachnik and K. Ueda: Phys. Rev. A **70** (2004) 040702.
24) H. Yoshida, J. Sasaki, Y. Kawabe, Y. Senba, A. De Fanis, M. Oura, S. Fritzsche, I. P. Sazhina, N. M. Kabachnik and K. Ueda: J. Phys. B **38** (2005) 465.
25) A. De Fanis, G. Prümper, U. Hergenhahn, E. Kukk, T. Tanaka, M. Kitajima, H. Tanaka, S. Fritzsche, N. M. Kabachnik and K. Ueda: J. Phys. B **38** (2005) 2229.
26) U. Hergenhahn, A. De Fanis, G. Prümper, A. K. Kazansky, N. M. Kabachnik and K. Ueda: J. Phys. B **38** (2005) 2843.
27) U. Hergenhahn, A. De Fanis, G. Prümper, A. K. Kazansky, N. M. Kabachnik and K. Ueda: Phys. Rev. A **73** (2006) 022709.
28) M. Kitajima, H. Yoshida, A. De Fanis, G. Prümper, U. Hergenhahn, E. Kukk, T. Tanaka, K. Nakagawa, H. Tanaka, S. Fritzsche, I. P. Sazhina, N. M. Kabachnik and K. Ueda: to be published in J. Phys. B **39** (2006).
29) R. Camilloni, M. Zitnik, C. Comicioli, K. C. Prince, M. Zacchigna, C. Crotti, C. Ottaviani, C. Quaresima, P. Perfetti and G. Stefani: Phys.

Rev. Lett. **77** (1996) 2646.

30) S. E. Canton-Rogan, A. A. Wills, T. W. Gorczyca, M. Wiedenhoeft, O. Nayandin, C.-N. Liu and N. Berrah: Phys. Rev. Lett. **85** (2000) 3113.

31) R. R. T. Marinho, O. Björnholm, S. L. Sorensen, I. Hjelte, S. Sundin, M. Bässler, S. Svensson and A. Naves de Brito: Phys. Rev. A **63** (2001) 032514.

32) N. Saito, N. M. Kabachnik, Y. Shimizu, H. Yoshida, H. Ohashi, Y. Tamenori, I. H. Suzuki and K. Ueda: J. Phys. B **33** (2000) L729.

33) M. N. Piancastelli: J. Electron Spectrosc. Relat. Phenom. **107** (2000) 1.

34) E. Kukk, J. D. Bozek and N. Berrah: Phys. Rev. A **62** (2000) 032708.

35) O. Björnholm, M. Bässler, A. Ausmees, I. Hjelte, R. Feifel, H. Wang, C. Miron, M. N. Piancastelli, S. Svensson, S. L. Sorensen, F. Gel'mukhanov and H. Ågren: Phys. Rev. Lett. **84** (2000) 2826.

36) Y. Muramatsu, Y. Shimizu, H. Yoshida, K. Okada, N. Saito, I. Koyano, H. Tanaka and K. Ueda: Chem. Phys. Lett. **330** (2000) 91.

37) I. Hjelte, M. N. Piancastelli, R. F. Fink, O. Björnholm, M. Bässler, R. Feifel, A. Giertz, H. Wang, K. Wiesner, A. Ausmees, C. Miron, S. L. Sorensen and S. Svensson: Chem. Phys. Lett. **334** (2001) 151.

38) M. N. Piancastelli, A. Kivimäki, V. Carravetta, I. Cacelli, R. Cimiraglia, C. Angeli, H. Wang, M. Coreno, M. de Simone, G. Turri and K. C. Prince: Phys. Rev. Lett. **88** (2002) 243002.

39) A. De Fanis, K. Nobusada, I. Hjelte, N. Saito, M. Kitajima, M. Okamoto, H. Tanaka, H. Yoshida, A. Hiraya, I. Koyano, M. N. Piancastelli and K. Ueda: J. Phys. B **35** (2002) L23.

40) A. Baev, F. Gel'mukhanov, P. Salek, H. Ågren, K. Ueda, A. De Fanis, K. Okada and S. L. Sorensen: Phys. Rev. A **66** (2002) 022509.

41) K. Ueda, M. Kitajima, A. De Fanis, T. Furuta, H. Shindo, T. Tanaka, H. Tanaka, K. Okada, R. Feifel, S. L. Sorensen, H. Yoshida and Y. Senba: Phys. Rev. Lett. **90** (2003) 233006.

42) M. Kitajima, K. Ueda, A. De Fanis, T. Furuta, H. Shindo, H. Tanaka, K. Okada, R. Feifel, S. L. Sorensen, F. Gel'mukhanov, A. Baev and H. Ågren: Phys. Rev. Lett. **91** (2003) 213003.

43) R. Feifel, K. Ueda, A. De Fanis, K. Okada, S. Tanimoto, T. Furuta, H. Shindo, M. Kitajima, H. Tanaka, O. Bjorneholm, L. Karlsson, S. Svensson and S. L. Sorensen: Phys. Rev. A **67** (2003) 032504.

44) K. Ueda, A. De Fanis, N. Saito, M. Machida, K. Kubozuka, H. Chiba, Y. Muramatsu, Y. Sato, A. Czasch, O. Jagutzki, R. Dörner, A. Cassimi, M. Kitajima, T. Furuta, H. Tanaka, S. L. Sorensen, K. Okada, S. Tanimoto, K. Ikejiri, Y. Tamenori, H. Ohashi and I. Koyano: Chem. Phys. **289** (2003) 135.

45) S. Sorensen, T. Tanaka, R. Feifel, J. H. D. Eland, M. Kitajima, H. Tanaka, R. Sankari, A. De Fanis, M. N. Piancastelli, L. Karlsson and K. Ueda: Chem. Phys. Lett. **398** (2004) 168.

46) M. N. Piancastelli, V. Carravetta, I. Hjelte, A. De Fanis, K. Okada, N. Saito, M. Kitajima, H. Tanaka and K. Ueda: Chem. Phys. Lett. **399** (2004) 426.

47) M. N. Piancastelli, R. Sankari, S. Sorensen, A. De Fanis, H. Yoshida, M. Kitajima, H. Tanaka and K. Ueda: Phys. Rev. A **71** (2005) 010703.

48) A. De Fanis, Y. Tamenori, M. Kitajima, H. Tanaka and K. Ueda: in *Proc. Int. Conf. Electron and Photon Impact Ionization and Related Topics 2004, Louvain-la-Neuve, 1–3 July 2004*, ed. B. Piraux (IOP Publishing, Bristol, 2005) IOP Conference Series, No. 183, p. 63.

49) I. Hjelte, L. Karlsson, S. Svensson, A. De Fanis, V. Carravetta, N. Saito, M. Kitajima, H. Tanaka, H. Yoshida, A. Hiraya, I. Koyano, K. Ueda and M. N. Piancastelli: J. Chem. Phys. **122** (2005) 084306.

50) T. Tanaka, H. Shindo, C. Makochekanwa, M. Kitajima, H. Tanaka, A. De Fanis, Y. Tamenori, K. Okada, R. Feifel, S. Sorensen, E. Kukk and K. Ueda: Phys. Rev. A **72** (2005) 022507.

51) G. Prümper, K. Ueda, Y. Tamenori, M. Kitajima, N. Kuze, H. Tanaka, C. Makochekanwa, M. Hoshino and M. Oura: Phys. Rev. A **71** (2005) 052704.

52) H. Ohashi, E. Ishiguro, Y. Tamenori, H. Kishimoto, M. Tanaka, M. Irie, T. Tanaka and T. Ishikawa: Nucl. Instrum. Methods Phys. Res., Sect. A **467–468** (2001) 529.

53) H. Ohashi, E. Ishiguro, Y. Tamenori, H. Okumura, A. Hiraya, H. Yoshida, Y. Senba, K. Okada, N. Saito, I. H. Suzuki, K. Ueda, T. Ibuki, S. Nagaoka, I. Koyano and T. Ishikawa: Nucl. Instrum. Methods Phys. Res., Sect. A **467–468** (2001) 533.

54) M. Breinig, M. H. Chen, G. E. Ice, F. Parente and B. Crasemann: Phys. Rev. A **22** (1980) 520.

55) U. Fano and J. W. Cooper: Rev. Mod. Phys. **40** (1968) 441.

56) U. Fano: Phys. Rev. **124** (1961) 1866.

57) Y. Shimizu, H. Ohashi, Y. Tamenori, Y. Muramatsu, H. Yoshida, K. Okada, N. Saito, H. Tanaka, I. Koyano, S. Shin and K. Ueda: J. Electron Spectrosc. Relat. Phenom. **114–116** (2001) 63.

58) T. Tanaka and H. Kitamura: J. Synchrotron Radiat. **3** (1996) 47.

59) H. Yoshida, K. Ueda, N. M. Kabachnik, Y. Shimizu, Y. Senba, Y. Tamenori, H. Ohashi, I. Koyano, I. H. Suzuki, R. Hentges, J. Viefhaus and U. Becker: J. Phys. B **33** (2000) 4343.

60) J.-E. Rubensson, M. Neeb, A. Bringer, M. Biermann and W. Eberhardt: Chem. Phys. Lett. **257** (1996) 447.

61) A. Albiez, M. Thoma, W. Weber and W. Mehlhorn: Z. Phys. D **16** (1990) 97.

62) N. M. Kabachnik, J. Tulkki, H. Aksela and S. Ricz: Phys. Rev. A **49** (1994) 4653.

63) N. M. Kabachnik and I. P. Sazhina: J. Phys. B **9** (1976) 1681.

64) A. F. Starace: Phys. Rev. A **16** (1977) 231.

65) Y. Tamenori, M. Kitajima, A. De Fanis, H. Shindo, T. Furuta, M. Machida, M. Nagoshi, K. Ikejiri, H. Yoshida, H. Ohashi, I. Koyano, H. Tanaka, P. Baltzer and K. Ueda: in *Proc. Int. Conf. X-ray and Inner-Shell Processes*, ed. A. Bianconi, A. Marcelli and N. L. Saini (AIP, New York, 2003) AIP Conference Proceedings, Vol. 652, p. 71.

66) M. Pahler, C. D. Caldwell, S. J. Schaphorst and M. O. Krause: J. Phys. B **26** (1993) 1617.

67) G. B. Armen and F. P. Larkins: J. Phys. B **24** (1991) 741.

68) C. Sinanis, G. Aspromallis and C. Nicolaides: J. Phys. B **28** (1995) L423.

69) W. Eberhardt, S. Bernstorff, H. W. Jochims, S. B. Whitfield and B. Crasemann: Phys. Rev. A **38** (1988) 3808.

70) J. Tulkki, T. Åberg, S. B. Whitfield and B. Crasemann: Phys. Rev. A **41** (1990) 181.

71) V. Schmidt: *Electron Spectrometry of Atoms using Synchrotron Radiation* (Cambridge University Press, Cambridge, 1997) p. 152.

72) A. Russek and W. Mehlhorn: J. Phys. B **19** (1986) 911.

73) W. Persson: Phys. Scr. **3** (1971) 133.

74) S. O. Kastner, A. K. Bathia and L. Cohen: Phys. Scr. **15** (1977) 259.

75) P. Bolognesi, L. Avaldi, D. R. Cooper, M. Coreno, R. Camilloni and G. C. King: J. Phys. B **35** (2002) 2927.

76) M. Neeb, J.-E. Rubensson, M. Biermann and E. Eberhardt: J. Electron Spectrosc. Relat. Phenom. **67** (1994) 261.

77) S. J. Osborne, A. Ausmees, S. Svensson, A. Kivimäki, O.-P. Sairanen, A. Naves de Brito, H. Aksela and S. Aksela: J. Chem. Phys. **102** (1995) 7317.

78) E. Kukk, J. D. Bozek, W.-T. Cheng, R. F. Fink, A. A. Wills and N. Berrah: J. Chem. Phys. **111** (1999) 9642.

79) M. N. Piancastelli, M. Neeb, A. Kivimäki, B. Kempgens, H. M. Köppe, K. Maier and A. M. Bradshaw: Phys. Rev. Lett. **77** (1996) 4302.

80) V. Carravetta, F. Kh. Gel'mukhanov, H. Ågren, S. Sundin, S. J. Osborne, A. Naves de Brito, O. Björnholm, A. Ausmees and S. Svensson: Phys. Rev. A **56** (1997) 4665.

81) M. Coreno, M. de Simone, K. C. Prince, R. Richter, M. Vondracek, L. Avaldi and R. Camilloni: Chem. Phys. Lett. **306** (1999) 269.

82) K. P. Huber and G. Herzberg: *Molecular Spectra and Molecular Structure IV* (Van Nostrand, New York, 1979).

83) K. Kuchitsu: *Structure of Free Polyatomic Molecules—Basic Data* (Springer, Berlin, 1998) p. 58.

84) G. Herzberg: *Molecular Spectra and Molecular Structure III, Electronic Spectra and Electronic Structure of Polyatomic Molecules* (Van Nostrand, New York, 1966) p. 402.

85) J. Adachi, N. Kosugi and A. Yagishita: J. Phys. B **38** (2005) R127, and references therein.

86) R. Sankari, M. Ehara, H. Nakatsuji, Y. Senba, K. Hosokawa, H. Yoshida, A. De Fanis, Y. Tamenori, S. Aksela and K. Ueda: Chem. Phys. Lett. **380** (2003) 647.

87) A. Cesar, H. Ågren and V. Carravetta: Phys. Rev. A **40** (1989) 187.

88) M. N. Piancastelli, A. Hempelmann, F. Heiser, O. Geßner, A. Rüdel and U. Becker: Phys. Rev. A **59** (1999) 300.

89) J. E. Reutt, L. S. Wang, Y. T. Lee and D. A. Shirley: J. Chem. Phys. **85** (1986) 6928.

90) W. C. Stolte, M.-M. Sant'Anna, G. Ohrwall, I. Dominguez-Lopez, M. N. Piancastelli and D. W. Lindle: Phys. Rev. A **68** (2003) 022701.

91) M. N. Piancastelli: J. Electron Spectrosc. Relat. Phenom. **100** (1999) 167.

92) W. Domcke and L. S. Cederbaum: Chem. Phys. **25** (1977) 189.

93) K. Ueda, Y. Shimizu, H. Chiba, M. Okunishi, K. Ohmori, J. B. West, Y. Sato, T. Hayaishi, H. Nakamatsu and T. Mukoyama: Phys. Rev. Lett. **79** (1997) 3371.

94) K. Okada, Y. Tamenori, I. Koyano and K. Ueda: Surf. Rev. Lett. **9** (2002) 89.

95) O. Kugeler, G. Prümper, R. Hentges, J. Viefhaus, D. Rolles, U. Becker, S. Marburger and U. Hergenhahn: Phys. Rev. Lett. **93** (2004) 033002.

96) G. Prümper, Y. Tamenori, A. De Fanis, U. Hergenhahn, M. Kitajima, M. Hoshino, H. Tanaka and K. Ueda: J. Phys. B **38** (2005) 1.

97) G. Prümper, K. Ueda, U. Hergenhahn, A. De Fanis, Y. Tamenori, M. Kitajima, M. Hoshino and H. Tanaka: J. Electron Spectrosc. Relat. Phenom. **144–147** (2005) 227.

98) see http://roentdek.com for details on the detectors.

99) see http://www.gpta.de for details on the HV pulse generator.

Kiyoshi Ueda was born in Osaka prefecture, Japan in 1954. He obtained his B.E. (1977), M.E. (1979) and Ph. D (1982) degrees from Kyoto University. He was a research associate (1982–1990), an associate professor (1990–2001) at Research Institute for Scientific Measurements, Tohoku University, and an associate professor (2001–2003) at Institute of Multidisciplinary Science for Advanced Materials, Tohoku University. Since 2003 he has been a professor at Institute of Multidisciplinary Science for Advanced Materials, Tohoku University. He has worked on atomic, molecular, and optical physics as well as physical chemistry. His current research is focused on spectroscopy and reaction dynamics of excited and/or transient species, as well as optical control of the reaction, using various light sources such as synchrotron radiation and lasers.